SPIN POLARIZED TUNNELING IN LARGE AREA MESAS OF SUPERCONDUCTING $Bi_2Sr_2CaCu_2O_{8+d}$ FOR TERAHERTZ EMISSION

A Thesis submitted to
The Graduate School of Engineering and Science of
İzmir Institute of Technology
in Partial Fulfillment of the Requirements for the Degree of

MASTER OF SCIENCE

in Physics

by
Fulya TÜRKOĞLU

July 2010
İZMİR

We approve the thesis of **Fulya TÜRKOĞLU**

_____

Assoc. Prof. Dr. Lütfi ÖZYÜZER
Supervisor

_____

Assoc. Prof. Dr. M. Salih DİNLEYİCİ
Committee Member

_____

Prof. Dr. M. Eyyüphan YAKINCI
Committee Member

01 July 2010

_____

Prof. Dr. Nejat BULUT
Head of the Department of Physics

_____

Assoc. Prof. Dr. Talat YALÇIN
Dean of the Graduate School of Engineering and Sciences

ACKNOWLEDGEMENTS

First of all, I would like to express my gratitude to Assoc. Professor Lütfi Özyüzer for giving me the possibility of carrying out this work under his supervision. I appreciate him, for his instructive guidance, inspiring suggestions, encouragement and understanding throughout the preparation of this thesis.

I would like to acknowledge Prof. Huabing Wang for providing us high quality Bi2212 single crystals. I am also thankful to Sascha Preu, Daniel Ploss and Stefan Malzer from Max Planck Optics Group for their helps in the interferometer measurements.

I wish to extend my thanks to İzmir Institute of Technology for providing Research Assistantship throughout my graduate study. I am also very thankful to all colleagues from İzmir Institute of Technology and our group members, especially Yasemin Demirhan and Yılmaz Şimşek for their helps and creating a nice environment while studying together.

I would like to express my deepest thanks to Hasan Köseoğlu, for his love, support and encouragement over the past seven years, and for his unwavering belief in me even when I doubted myself. Last, but not least I want to thank my family for their unconditional love, unending support and understanding during my whole life and providing me with more than I can ever repay them for.

ABSTRACT

SPIN POLARIZED TUNNELING IN LARGE AREA MESAS OF SUPERCONDUCTING $Bi_2Sr_2CaCu_2O_{8+d}$ FOR TERAHERTZ EMISSION

There is an increasing interest in science and technology of electromagnetic waves in terahertz frequency range (0.1-10 THz) because of their emerging application areas including physics, biology, chemistry, astronomy, medicine etc. The observation on generation of THz radiation emitted from lateral dimension of high temperature superconductor (HTS) $Bi_2Sr_2CaCu_2O_{8+\delta}$ (Bi2212) and responses to THz waves increase the importance of these HTSs. Single crystal of HTS Bi2212 forms natural superconductor-insulator-superconductor (SIS) layered junctions, which are called intrinsic Josephson junctions (IJJ). The stacks of IJJs in Bi2212 can be used such a voltage-frequency converter and their large energy gap allows the emissions at THz frequency range. Recently, it has been demonstrated that rectangular IJJ mesa structures of Bi2212 can be used as a source of continuous, coherent and polarized THz radiation. It was shown that all THz emitting mesas are below a certain underdoped level, which has relatively small critical current in contrast to optimally doped and overdoped Bi2212. In this work, rectangular Au/Co/Au/Bi2212 mesa structures with large areas and high thicknesses were fabricated on as-grown Bi2212 single crystals using standard photolithograph and Ar ion beam etching techniques. In order to characterize the mesas, c-axis resistance versus temperature (R-T) and current-voltage (I-V) characteristics were investigated. During I-V characterization, Si composite bolometer was used to detect the emission. We obtained small critical current from as-grown mesas due to injection of spin polarized current. We observed THz emission peak for one of the mesas which has low quasiparticle conductivity and low dissipation due to its small critical current density. It means that the adjustment of doping level can be eliminated for THz emission by the injection of spin polarized current through the c-axes of the as-grown mesas.

ÖZET

TERAHERTZ IŞIYAN BÜYÜK ALAN SÜPERİLETKEN $Bi_2Sr_2CaCu_2O_{8+d}$ MESALARIN SPİN POLARİZE TÜNELLEMESİ

Terahertz frekans aralığındaki (0.1-10 THz) elektromanyetik dalgalara fizik, biyoloji, kimya, tıp ve astronomiyi içeren uygulama alanlarından dolayı artan bir ilgi vardır. Yüksek sıcaklık süperiletkeni (YSS) $Bi_2Sr_2CaCu_2O_{8+\delta}$ (Bi2212) tek kristalinin yanal kenarlarından THz ışıması üretiminin gözlemlenmesi bu YSS'lerinin önemini arttırır. Bi2212 tek kristali özgün Josephson eklemleri (ÖJE) olarak adlandırılan doğal süperiletken-yalıtkan-süperiletken (SYS) katmanlı eklemlerinden oluşur. Bi2212 içerisindeki özgün Josephson eklem yığınları voltaj-frekans dönüştürücüsü olarak kullanılabilir ve geniş enerji aralıkları THz frekans aralığındaki ışımalara uygundur. Bi2212'nin dikdörtgen şeklindeki mesa yapılarının sürekli, koherent ve polarize THz ışıması kaynağı olarak kullanılabileceği kanıtlanmıştır. Tüm THz ışıyan mesaların optimally doped ve overdoped Bi2212 lere göre daha küçük bir kritik akıma sahip olan, belli bir underdoped seviyenin altında olduğu gösterilmiştir. Bu çalışmada, as-grown Bi2212 tek kristalleri üzerine standart fotolitografi ve Argon iyon demeti aşındırması teknikleri kullanılarak geniş alanlı ve yüksek kalınlıklı dikdörtgen Au/Co/Au/Bi2212 mesa yapıları oluşturuldu. Mesaları karakterize edebilmek için, c-ekseni direnç-sıcaklık (R-T) ve akım-gerilim (I-V) karakteristikleri incelendi. Akım- gerilim karakterizasyonu esnasında, ışımayı dedekte edebilmek için Si kompozit bolometre kullanıldı. As-grown mesalardan spin polarize akım enjeksiyonundan dolayı düşük kritik akım yoğunluğu elde ettik. Kritik akım yoğunluğunun az olmasından dolayı düşük sanki parçacık iletkenliği ve enerji yayılımı olan mesalardan birinde THz ışıma piki gözlemledik. Bu, as-grown mesaların c-ekseni boyunca spin polarize akım enjekte ederek, THz ışıması için doping seviyesinin ayarlanması gerekliliğinin elimine edilebileceğini gösterir.

TABLE OF CONTENTS

LIST OF FIGURES

Figure **Page**

LIST OF TABLES

Table **Page**

CHAPTER 1

INTRODUCTION

1.1. Superconductivity

The electrical resistance of some metals and alloys vanishes abruptly when they are cooled below a certain temperature. This phenomenon of superconductivity was discovered by Kamerlingh Onnes (Onnes 1911) in Leiden in 1911, after three years he first liquefied helium. At the critical temperature T_c, the material undergoes a phase transition from a state of normal electrical resistance to a superconducting state with no resistance. Thus, any small electrical current which may occur in the superconducting sample will not decay and persists as long as the sample temperature is kept below T_c.

The magnetic properties of superconductors attracted considerable attention through the 1920s and 1930s. A breakthrough came in 1933 when Meissner and Ochsenfeld (Meissner and Ochsenfeld 1933) showed that in magnetic fields below a certain threshold value the flux inside the superconductor was expelled, and this defined a new thermodynamic state and was not a consequence of infinite conductivity. The phenomenon became known as the Meissner effect and laid the foundation for a thermodynamic treatment of superconductivity. A breakthrough was made by Abrikosov who showed the existence of two types of superconductors and the vortex state, only found in Type-II superconductors (Abrikosov 1957). A Type I superconductor completely obeys Meissner effect but a Type II superconductor have two critical magnetic fields H_{c1} and H_{c2}. Below first critical magnetic field (H_{c1}) it expels magnetic field and above this value magnetic flux penetrate into the material in normal regions surrounded by superconducting ones. The material remains perfect conductor until applied magnetic field exceed second critical magnetic field (H_{c2}). Both H_{c1} and H_{c2} depend on temperature. In the mixed state, also called vortex state, the magnetic field penetrates into superconductor in quantized units of magnetic flux, $\Phi=h/2e=2.068\times10^{-15}$ Wb. Thus, in the mixed state there are normal regions surrounded by superconducting regions.

The microscopic theory of superconductivity was created by Bardeen, Cooper and Schrieffer in 1957 (Bardeen, et al. 1957). According to this so-called BCS–theory, the electrons form pairs, known as Cooper-pairs, due to interactions with the crystal lattice at low temperatures. Electrons in these Cooper-pairs have opposite values of momentum, meaning that the pairs themselves generally have zero orbital angular momentum. Additionally, the angular momenta add up to zero. The formation of Cooper-pairs leads to a superconducting energy gap, which means that single electrons cannot occupy states near the Fermi surface. Such energy gaps which are essentially equal to the energy needed to break up the Cooper-pairs show up clearly as jumps in the specific heat and thermal conductivity at the critical temperature T_c. The Ginzburg–Landau and London results fit well into the BCS formalism (Ginzburg and Landau 1950, London 1950). Experimentally, the energy gap varies with temperature that is also predicted by BCS theory. At T=0, the ratio $2\Delta(0)/k_BT_c$ variation with superconductor elements are typically between 3.2 and 4.6 but this radio predicted by BCS theory is equal to 3.5 (Wesche 1998). Much of the present theoretical debate centers on how well the BCS theory explains the properties of the new high temperature superconductors.

The one effect that played the decisive role in showing the way to the correct theory of superconductivity in metals was the isotope effect (Maxwell 1950, Reynolds, et al. 1950). A study of different superconducting isotopes of mercury established a relationship between the critical temperature and the isotope mass M: $T_cM^{1/2}$ = constant, which turned out to be valid for most of conventional superconductors. Even nowadays the isotope effect serves as an indicator of the BCS mechanism of superconductivity.

Another significant theoretical advancement came in 1962 when Brian Josephson, a graduate student at Cambridge University, predicted that the electrical current would flow between two superconducting materials, even when they are separated by a non-superconductor or a thin insulator (Josephson 1962). His prediction was later confirmed and won him a shared of the 1973 Nobel Prize in Physics with Leo Esaki and Ivar Giaever (Giaever did experiments on superconducting tunneling systems (Giaever 1960) before Josephson prediction). This tunneling phenomenon is today known as the “Josephson effect”. It plays a special role in superconducting applications and has been applied to electronic devices such as the Superconducting Quantum Interference Device (SQUID), an instrument capable of detecting even the weakest magnetic fields.

1.2. High Temperature Superconductors

The highest transition temperature of superconductors was not over 23.2 K found in the compound Nb_3Ge until 1986 when K. Alex Müller and J. Georg Bednorz discovered that a mixture of lanthanum, barium, copper and oxygen displayed indications of a superconducting transition at temperatures above 30 K (Bednorz and Müller 1986). Their discovery led them to receive 1987 Nobel Prize. By the beginning of 1987, scientists had fabricated the lanthanum compound, which went superconducting at close to 40 K at ambient pressure and at up to 52 K under high pressure (Chu, et al. 1987a). A remarkable evolution came in 1987 with the discovery of the complex ceramic oxide superconductor $YBa_2Cu_3O_7$ which has a critical temperature of 92 K (Wu, et al. 1987). The importance of this discovery is based on the fact that the superconductivity can be maintained in cryostats with relatively cheap liquid nitrogen (which boils at 77 K) rather than liquid helium so that commercial applications of the superconductivity may become more widespread and common. Early in 1988, two superconducting phases were characterized as $Bi_2Sr_2CaCu_2O_{8+\delta}$ (Bi2212) and $Bi_2Sr_2Ca_2Cu_3O_{10+\delta}$ (Bi2223) with their T_c 95 K and 110 K, respectively (Maeda, et al. 1988). After a very short time, the critical temperature reached to 125 K with the discovery of thallium barium calcium copper oxide compound (TBCCO), $Tl_2Ba_2Ca_2Cu_3O_\delta$ (Tl2223) (Hazen, et al. 1988). To date the record at ambient pressure stands at 135K in $HgBa_2Ca_2Cu_3O_{8+\delta}$ (Hg1223) superconductor compound (Schilling, et al. 1993). The transition temperature of this material can be increased up to 160-165 K by the application of pressure (Gao, et al. 1994).

In January 2001, MgB_2 with T_c = 39 K was discovered (Nagamatsu, et al. 2001). Although MgB_2 obeys conventional models of superconductivity and has relatively basic structure if compared with the cuprates, it is occasionally referred to as a high-temperature superconductor because its T_c value of 39 K is above that historically expected for BCS superconductors. However, it is more generally regarded as the highest T_c conventional superconductor.

The 2006 discovery of superconductivity in the iron- and nickel-based layered compound LaOFeP did not receive much attention, since it occurred only below several Kelvin (Kamihara, et al. 2006). In 2008, F-doped LaOFeAs was found to be superconductor at approximately 43 K at under pressure (Takahashi, et al. 2008). In the same year, iron-based oxyarsenide $Sm[O_{1-x}F_x]FeAs$, with the onset resistivity transition

temperature at 55 K was discovered (Zhi-An, et al. 2008). This is currently the family with the second highest transition temperature, behind the cuprates. Figure 1.1 shows the superconducting critical temperature of several cuprates and some metallic superconductors as a function of the year of discovery.

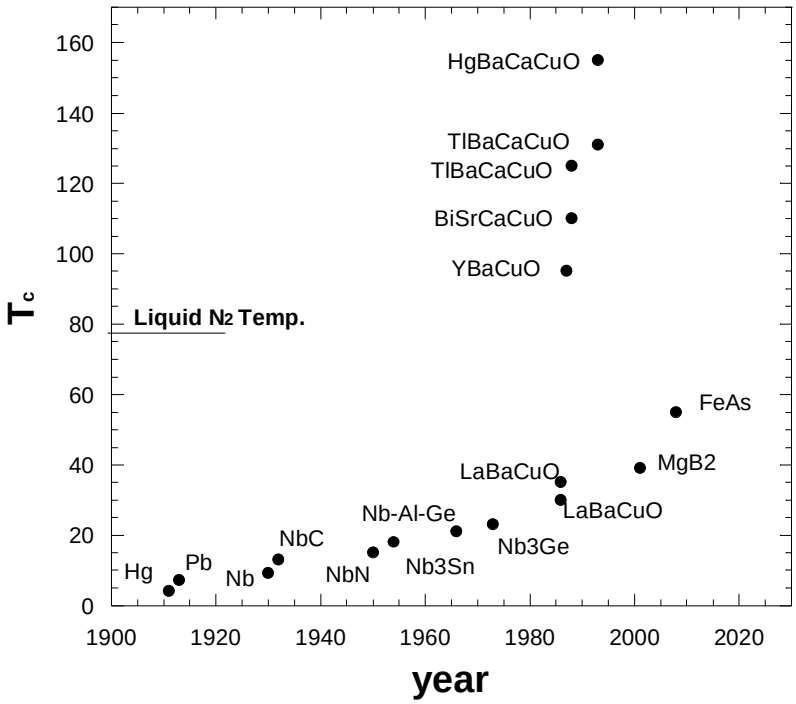

Figure 1.1. The critical temperature evolutions of several cuprates and some metallic superconductors

All known high temperature superconductors are Type-II superconductors. In contrast to Type-I superconductors, which expel all magnetic fields due to the Meissner Effect, Type-II superconductors allow magnetic fields to penetrate their interior in quantized units of flux, creating "holes" or "tubes" of normal metallic regions in the superconducting bulk. Consequently, high temperature superconductors can sustain much higher magnetic fields.

Although there are various instances of HTS, this work will focus on the basic features of cuprates. Cuprate superconductors differ in many important ways from conventional superconductors which are adequately explained by the BCS theory. Essentially all of the effects studied in conventional superconductors are also found in high T_c superconductors. However, in the later, some of these effects are exaggerated because of the higher temperatures, the small coherence length and the anisotropy.

The high temperature cuprate superconductors have layered perovskite-like crystal structures which consist of conducting CuO_2 planes separated by layers comprised of other elements and oxygen. It is believed that superconductivity and charge transport are mostly confined to the CuO_2 planes. Atomic planes of the remaining part, sandwiching the CuO_2 plane, also play an important role in that they accommodate additional oxygen atoms to provide charge carriers into CuO_2 planes and so they referred to as charge reservoirs. The multi-layered structures of cuprates make them highly anisotropic. In these multi-layered structures, there are two different crystalline directions (the in plane direction and the direction perpendicular to the planes or c-axis). In different crystalline directions, characteristic physical parameters such as critical fields, London penetration depth, superconducting coherence length, resistivity and energy gap also show anisotropic behaviors.

There are several families of cuprate superconductors and they can be categorized by the elements they contain and the number of adjacent CuO_2 layers in each superconducting block. For example Bi-Sr-Ca-Cu-O system can alternatively be referred to Bi2201/Bi2212/Bi2223 depending on the number of layers in each superconducting block. In general, the critical temperatures of cuprate superconductors are closely correlated with the number of CuO_2 layers in the unit cell (N_l) and the charge carrier concentration in the layers. At fixed doping level, T_c first increases by increasing the number of CuO_2 layers, reaching the maximum at $N_l=3$, and then decreases. In most superconducting cuprates, by changing the doping level at fixed N_l, the T_c dependence has the bell-like shape. So, the maximum T_c can only be obtained when all necessary parameters have their optimal values.

After the discovery of high temperature superconductivity in cuprates, considerable number of theoretical models of the mechanism of the high temperature superconductivity was proposed, but even today there is no consensus among theoretical physicists. There are so many various kinds of interactions in such complicated systems-electron-phonon interactions, spin-spin interactions, charge density waves, spin density waves and so on.

1.3. Josephson Effect

Since the discovery and explanation of superconductivity, many applications have been proposed and exploited. Some of the more interesting applications have made use of quantum mechanical effects in superconductivity. One such example is the Josephson junction which consists of two superconductors that are separated by a very thin electrically insulating barrier. From his calculations using the BCS theory, Josephson discovered that the probability of a Cooper pair tunneling through the barrier was the same as that for a single electron. (Josephson 1962). The reason is that the tunneling for a Cooper pair is an ordered, coherent process. In other words, we should not imagine the situation to be two electrons' matter waves leaking across the insulating barrier. Instead, it is the macroscopic wave function that tunnel from one superconductor to the other. Soon after the prediction, Philip Anderson and John Rowell had experimentally confirmed the existence of Cooper pair tunneling using a tin-tin oxide-lead junction (Anderson and Rowell 1963). The zero-voltage current flow resulting from the tunneling of Cooper pairs is known as the DC Josephson effect and depends on the phase difference, $\phi = \theta_2 - \theta_1$, of the superconducting effective wave functions on both sides of the barrier as

$$I_s = I_c \sin\phi \tag{1.1}$$

where I_c is the maximum dissipationless current, which can flow through the junction and is called critical current. It is specific for each junction and depends on superconducting materials, the thickness of the barrier and the junction area. As long as the amplitude of a constant current flowing through the barrier does not exceed the critical current I_c, there is no voltage drop across the junction. For currents above the critical value, the junction switches into a voltage state. For a tunneling junction with identical conventional superconductors, the temperature dependence of the critical Josephson current was derived in the framework of the BCS theory by Ambegaokar and Baratoff (Ambegaokar 1963)

$$I_c(T) = \frac{\pi}{2e}\frac{\Delta(T)}{R_n}\tanh\left(\frac{\Delta(T)}{k_B T}\right) \tag{1.2}$$

where R is the normal state resistance of the tunnel barrier and Δ(T) is the temperature-dependent energy gap, as given by the BCS theory. Equation 1.2 follows that at low temperatures; the critical current I_c is related to the normal tunnel resistance R_n as

$$I_c(0) = \frac{\pi}{2e}\frac{\Delta(0)}{R_n} \tag{1.3}$$

where Δ is given in eV.

Josephson also predicted that if a constant nonzero voltage is applied across the insulating barrier, an alternating Josephson current occurs (Josephson 1964, Josephson 1974). The oscillating current of Cooper pairs that flows when a steady voltage is maintained across a tunnel barrier is known as the AC Josephson effect. The oscillation frequency is given by

$$\frac{\partial\phi}{\partial t} = \frac{2\pi}{\Phi_0}V = \frac{2e}{\hbar}V \tag{1.4}$$

where Φ_0=h/2e=2.07x10^{-15} V s is the magnetic flux quantum, e is the electron charge and h is Planck's constant. From Equation 1.4, we see that a voltage drop of 1 mV across the barrier will result in an oscillating current with a frequency of ω=3.035 10^{12} s^{-1} or f=ω/2π=483.1 GHz, manifesting itself by the emission of electromagnetic radiation. This so-called AC Josephson effect was first observed in indirect experiments by Shapiro (Shapiro 1963) and directly in the radiation measurements by Giaever (Giaever 1965).

1.4. Terahertz Radiation

Terahertz (THz) waves, or submillimeter/far-infrared waves, refer to electromagnetic radiation in the frequency interval from 0.1 to 10 THz. These frequencies correspond to wavelengths between 3 mm and 0.03 mm. The terahertz regime of the electromagnetic spectrum lies in the gap between microwaves and infrared. This spectral region has long been considered the last remaining scientific gap in the electromagnetic spectrum. This so-called 'terahertz gap' has been defined by the

relative lack of convenient and inexpensive sources, detectors, other components for the manipulation of terahertz waves. Lately, however, many new advances in the technology for generation, manipulation, and detection of terahertz radiation have revolutionized the field. Much of this interest has been inspired by its ability to enable a host of new applications.

Terahertz radiation possesses unique characteristics not found in other portions of the spectrum. THz waves have low photon energies (1 THz = 4.1 meV), one million times weaker than X-rays, and do not cause harmful photoionization in biological tissues (Kawase 2004). Because terahertz radiation is absorbed by water, it can also detect differences in water content and density of a tissue. The way in which terahertz waves interact with living matter has potential for highlighting the early signs of tooth decay and skin or breast cancer, or understanding cell dynamics with a safer and less invasive or painful system using imaging. Their ability to penetrate materials that are usually opaque to both visible and infrared radiation also makes these waves so fascinating to scientists. For example, terahertz waves can pass through fog, clothing, fabrics, plastics, wood, paper, ceramic and even a few centimeters of brick. It matches in frequency the motion of an enormous range of molecules in many chemical and biological materials. The transmitted and reflected THz spectra of these materials contain THz absorption fingerprints characterizing these THz vibrational modes and provide spectroscopic information (Fischer, et al. 2005). Spectroscopy in terahertz radiation makes the technique particularly useful for pharmaceutical applications where rapidly and precisely identifying the makeup of drugs is essential. Owing to these advantages, THz technologies have been considered competitive methods for inspecting hidden explosives, chemical/biological threats and defects for defense and security applications (Arnone, et al. 1999). Also, potential uses exist in ultra-high bandwidth wireless communication networks, vehicle control, atmospheric pollution monitoring and inter-satellite communication (Tonouchi 2007).

Some images about the some part of the applications of THz radiation area shown in the Figure 1.2.

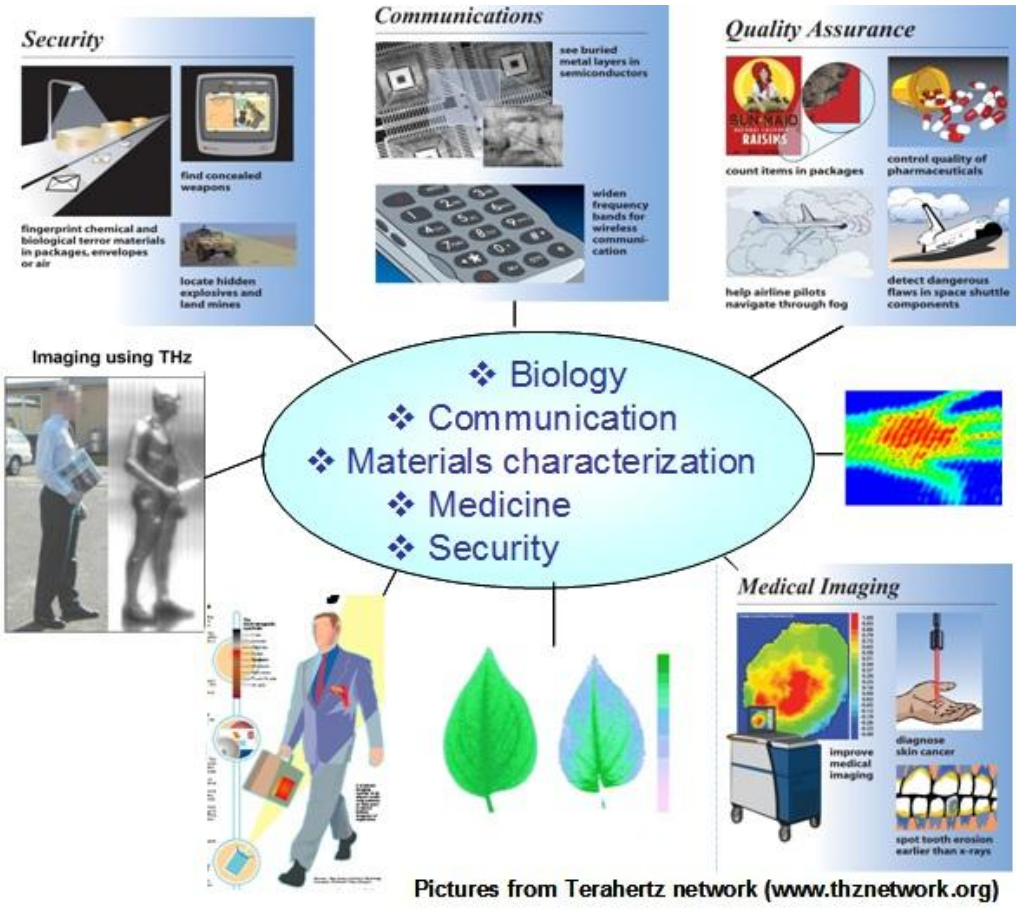

Figure 1.2. Some of the applications of THz radiation
(Source: THznetwork 2010)

Large scale real world applications will inevitably require cheap, tunable, compact, continuous wave (CW), solid-state terahertz wave sources with practical emission power. There are some available CW sources such as quantum cascade lasers that only work above 1.2 THz (Wade, et al. 2009). Multiplication of Gunn diodes produces low output powers. Backward wave oscillators are bulky and have low output power at higher frequencies. Optically-pumped THz gas lasers are also bulky and not tunable. Free electron lasers are the most powerful sources available, producing either CW or pulsed beams of coherent THz waves (Saldin, et al. 2000). However, their bulky size and high cost prevent their use in nonlaboratory applications. Schottky diodes are fairly compact but lacking in frequency agility and their cost is very high.

High temperature superconductor Bi2212 single crystals could provide a solution to limitations of current sources. These crystals comprise stacks of Josephson junctions that exhibit a unique electrical property: when an external voltage is applied, an alternating current will flow back and forth across the junctions at a frequency

proportional to the strength of the voltage; this phenomenon is known as the Josephson Effect. These alternating currents then produce electromagnetic fields whose frequency is tuned by the applied voltage. Even a small voltage around two mVs per junction can induce frequencies in the terahertz range. There is more about the detail of the generation of THz waves from HTS Bi2212 in Chapter 2.

1.5. Spin-Polarized Current Injection

The first step in understanding the effects of the spin on a spin polarized current was suggested by Mott (Mott 1936), who introduced the idea of 2 population of electrons with different spins (majority and minority) in a current to explain the unusual behavior of resistance in ferromagnetic metals on external magnetic field at sufficiently low temperatures. The early experiments involving spin related effects demonstrated that electrical currents from ferromagnets may become spin polarized, and the spin-polarized current may tunnel through an insulating barrier into a superconductor (Tedrow and Meservey 1973). The effects of the spin polarized current in superconducting (Aronov 1976a) and normal (Aronov 1976b) metals were first proposed by Aronov. He predicted that a spin polarized current from the ferromagnetic metal would produce a nonequilibrium magnetization in the normal or superconducting metal so there would be a shift in the chemical potentials of the spin up and spin down electrons. This effect is known as spin accumulation.

In high temperature superconductors, injection of spin polarized current from ferromagnetic films results in strong suppression of the superconducting critical current and significant modification to the quasiparticle density of states (DOS) (Fu 2002). The experimental findings are attributed to the dynamic pair-breaking effects of spin polarized quasiparticle as a result of excess magnetic moments and quasiparticle redistribution.

The spin-polarized current injection into the high T_c cuprates has attracted much research interest because it can provide key information on the superconducting mechanism as well as normal-state properties of cuprates. In particular, they in principle allow us to extract the bulk spin transport properties of the high T_c cuprates. In the normal state, such spin transport properties have been proposed as a probe of spin-charge separation due to the resonant-valence-bond (RVB) scenario. In the

superconducting state, they can provide more information and insight on the nature of the quasiparticles for the cuprates. In addition, the anisotropy of the spin transport properties should shed new light on the nature of the c-axis transport properties of cuprates such as Bi2212. Spin-injection into superconductors also provides a setting to study the phenomenon of spatial separation of charge and spin currents. Furthermore, investigating the characteristic spin and charge relaxation and transport processes in the F-I-S devices can be unique vehicle for probing nonequilibrium superconductivity and possibly the pairing mechanism in the cuprates (Fu 2002).

CHAPTER 2

THEORETICAL BACKGROUND

2.1. Properties of $Bi_2Sr_2CaCu_2O_{8+\delta}$ Single Crystal

The bismuth based family of HTSs generally formulated by $Bi_2Sr_2Ca_{n-1}Cu_nO_{2n+4+\delta}$ (BSCCO). 'n' represents the number of perovskite units or equivalently the number of consecutive copper oxide layers in the unit cell. The family of bismuth cuprates consists of three members which are $Bi_2Sr_2CuO_{6+\delta}$ (Bi2201) for n=1 with $T_c \leq 20$ (Akimitsu, et al. 1987), $Bi_2Sr_2CaCu_2O_{8+\delta}$ (Bi2212) for n=2 with $T_c \approx 95$ K and $Bi_2Sr_2Ca_2Cu_3O_{10+\delta}$ (Bi2223) for n=3 with T_c=110 K (Maeda, et al. 1988) respectively. These structures have layered atomic arrangement with planes of weak bonding, the $(BiO)_2$ (Romano, et al. 1998) and have in common both the conduction layer and charge reservoir layer. The number of CuO_2 layer is the difference among them.

Among the cuprates, or more specifically within the BSCCO family, more investments and efforts have been devoted on Bi2212 due to its better properties. The most important advantage of this material is that growing of high quality mm-sized single crystal without any macroscopic defects or dislocations is relatively easy. The bonds between BiO layers in the crystal are weak so the single crystal can be cleaved along the ab-plane without damaging the basic structure of the compound. After the cleavage, flat and convenient regions on the Bi2212 crystal are obtained. Moreover, its transition temperature can be varied by adding excess oxygen atoms or by reducing oxygen atoms without changing crystalline structure. The optimally doped samples of Bi2212 have approximately an onset critical temperature of 95 K which is the maximum value of T_c for this compound.

The Ginzburg-Landau parameter, κ, is larger than 100 for the Bi2212 compound; which means that it exhibits strong type II superconducting behavior. Associated with this parameter, it has large penetration depth λ_{ab}=200-300 nm, λ_c=15-150 µm and extremely short coherence length ξ_{ab} and ξ_c is 2 nm and 0.1 nm respectively (Buckel 2004).

The structure of Bi2212 single crystal is formed by stacked series arrays of intrinsic Josephson tunnel junctions along the direction of crystal c-axis. Sequence of its stacking atomic layers is like that; $(BiO)_2$ / SrO / $(CuO)_2$ / Ca / $(CuO)_2$ / SrO / $(BiO)_2$ / SrO / $(CuO)_2$ / Ca / $(CuO)_2$ / SrO / $(BiO)_2$. Due to this layered structure, crystal shows excessively anisotropic properties in different crystalline directions. In order to explain the mechanism of this material multilayer model and proximity model was developed (Yurgens, et al. 1996a). Multilayer model is represented in Figure 2.1.

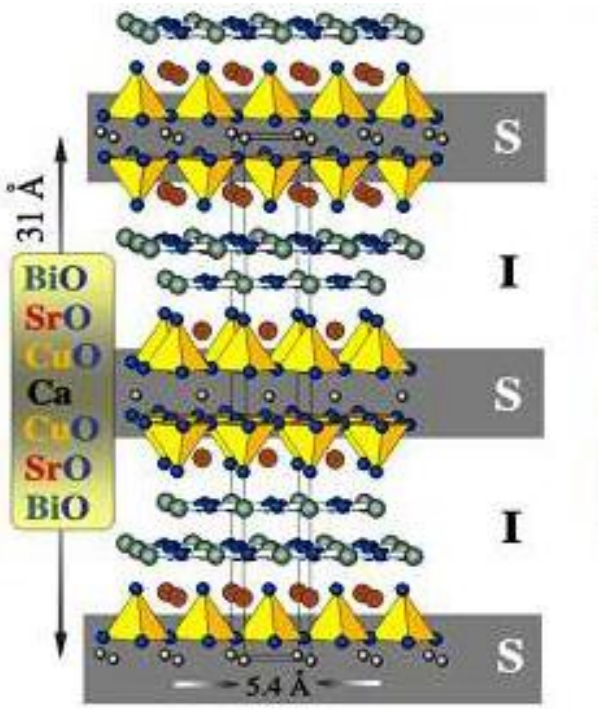

Figure 2.1. The crystal structure of Bi2212
(Source: Yurgens, et al. 1996a)

According to the multilayer model, Bi2212 single crystals act as stacks of Josephson coupled Cu-O double layers with the thickness of 0.3 nm separated by non-superconducting Sr-O and Bi-O layers with the thickness of 1.2 nm. This configuration forms natural Josephson tunnel junctions array going on like SISIS... inside the single crystal and enables to observe both DC and AC Josephson effects. It is believed that superconductivity and charge transport are mostly confined to the double Cu-O layers in which coupling occur. Atomic planes of the remaining part, Sr-O and Bi-O intermediate planes also play an important role in that they accommodate additional oxygen atoms to provide charge carriers into CuO_2 planes and so they referred to as charge reservoirs. As mentioned above, the c-axis Ginzburg-Landau coherence length of Bi2212 is

approximately 0.1 nm which is relatively smaller than the spacing between two adjacent CuO_2 layers. This makes Josephson tunneling of Cooper pairs hard across the insulating layer. (Yurgens, et al.1996a).

2.2. Doping Dependence of Bi2212

The parent states of each family of cuprates are antiferromagnetic Mott insulators with one hole per planar copper (Taillefer, et al. 1997). A mott insulator is a material in which the conductivity vanishes as temperature tends to zero. These insulators are transformed into metals and then superconductors by doping with charge carriers. As a function of increasing carrier concentration, they all have an antiferromagnetic phase near zero doping, followed by an insulating phase, then the superconducting transition temperature rises from zero to a maximum and finally drops to zero again. It is widely believed that all cuprates have the same phase diagram schematically shown in Figure 2.2. The two regions of the diagram, antiferromagnetic insulating state (AF) with hole doping $p \leq 0.02$ and the superconducting state (SC) p is between 0.06 and 0.26 are well-established. The insulating phase is usually called as undoped region. The materials are said to be underdoped where T_c is an increasing function of carrier concentration. They are optimally doped where T_c reaches its maximum and they are overdoped for larger carrier concentration. In the underdoped regime there are a variety of crossover phenomena observed at temperatures above T_c. These phenomena are associated with the opening of a pseudo gap.

Carrier concentrations of superconducting cuprates can be varied by adding excess oxygen atoms or by reducing oxygen atoms without changing crystalline structure. Although hole-doping is the rule in high-T_c superconductors there are some cases where the mobile charges are electrons. The phase diagram of the electron-doped HTS is qualitatively similar to the phase diagram of the hole-doped HTS.

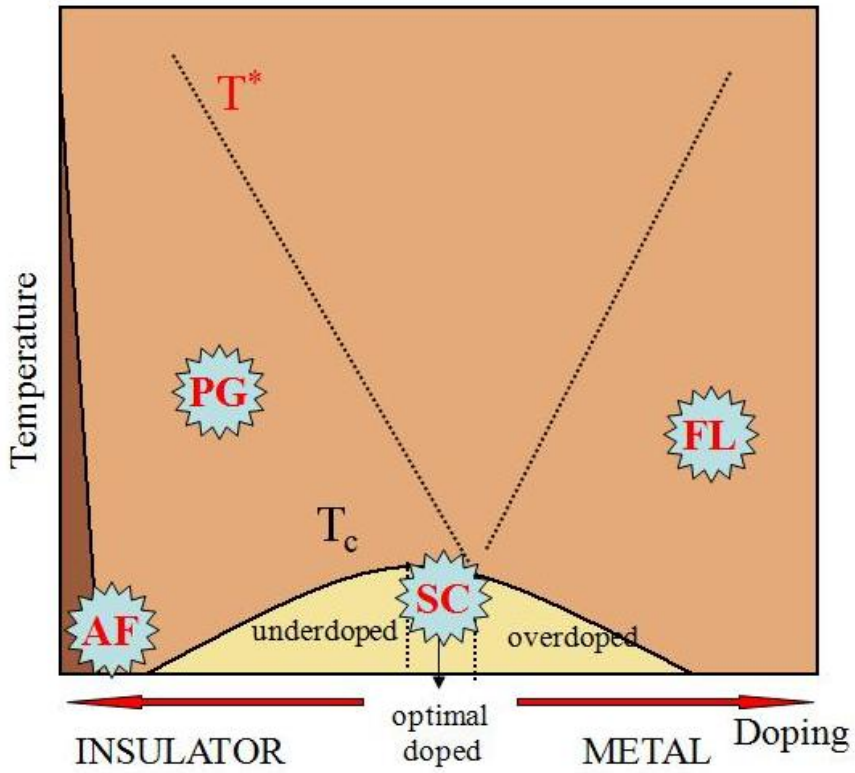

Figure 2.2. Typical overall phase diagram with doping in high-Tc cuprate superconductors

The doping dependence of various superconducting properties of Bi2212 single crystal such as energy gap studied extensively. Superconducting energy gaps of the underdoped $Bi_2Sr_2CaCu_2O_{8+d}$ single crystals are larger than optimally doped crystals and the trend of decreasing energy gap with increasing hole doping continue into the overdoped region (Miyakawa, et al. 1998). The optimally doped samples of Bi2212 have approximately an onset critical temperature of 95 K. Figure 2.3 shows the temperature dependence of c-axis resistivity, ρ_c, of Bi2212 single crystal with various doping level. As it can be seen in the figure, overall magnitude of c-axis resistivity of the crystal increases with decreasing doping level (Watanable, et al. 1997). At variation of oxygen level from the optimally doped to overdoped, c-axis resistivity of the crystal gradually start to exhibit metallic behavior. Moreover, Josephson critical current density of the crystal increases significantly as the doping level increases (Suzuki, et al. 2009).

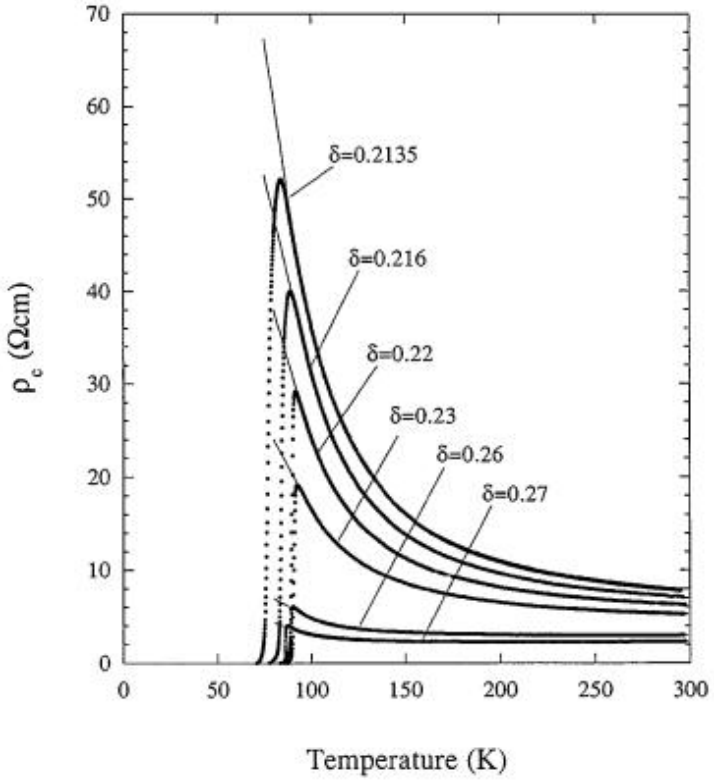

Figure 2.3. Out-of-plane resistivity (ρ_c) of a $Bi_2Sr_2CaCu_2O_{8+\delta}$ single crystal versus temperature for various oxygen contents (δ) (Source: Watanable, et al. 1997)

2.3. Tunneling

The concept of tunneling has been known as quantum mechanical process. From quantum mechanics we know that a particle such as an electron can be described by a wave function and it has a small, but nonzero, probability of entering a classically forbidden region. Consequently, the particle may tunnel through a potential barrier which separates two classically allowed regions. The tunneling probability can be increased by making the potential barrier width small enough (nearly 1 nm) and having many carriers available for tunneling. Electron tunneling was for the first time observed experimentally in junctions between two semiconductors by Esaki in 1957 (Esaki 1957). In 1960, Ivar Giaever performed tunneling measurements to observe electron tunneling between normal metal and a superconductor (Giaever 1960b).

Different kinds of tunnel junctions such as NIN, SIN, SIS (N: normal metal, I: insulator, S: superconductor) can be created by interrupting two metal with an ultra thin

insulating layer. Within the independent particle approximation, the tunneling current from metal 1 to metal 2 is

$$I = c|T|^2 \int_{-\infty}^{\infty} N_1(E)N_2(E + eV)[f(E) - f(E + eV)]dE \qquad (2.1)$$

where c is a constant of proportionality, T is a constant tunneling matrix element, $N_1(E)$ and $N_2(E)$ are the density of states of the metals and f(E) is the Fermi-Dirac distribution function.

When both electrodes are normal metals, Equation 2.1 gives the tunneling current as

$$I_{nn} = c|T|^2 N_n(0)N_n(0)eV \equiv G_{nn}V \; : \; G_{nn}V = \frac{1}{R_{nn}}V \qquad (2.2)$$

so that the junction is ohmic. Now, without a voltage applied, their Fermi levels become equal as shown in Figure 2.4.a and no net charge transport can occur. When a small potential difference V is applied to the junction, the Fermi levels of the metals will shift apart by the amount of eV with respect to each other as shown in Figure 2.4.b, that the electrons are now able to tunnel from the top of the conduction band of the fixed metal to the empty continuum levels of the positively biased metal.

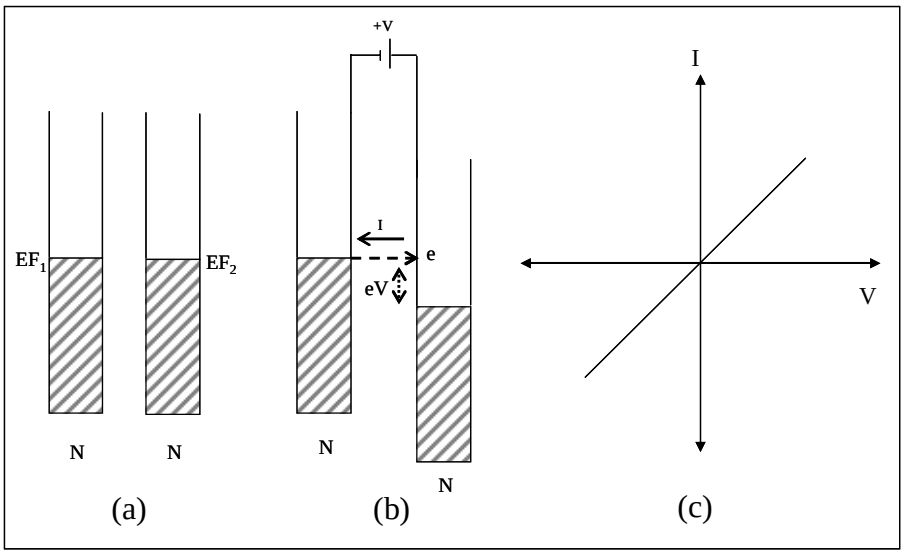

Figure 2.4. The NIN tunneling process and its current-voltage (I-V) characteristic at T= 0 K

It will be helpful to examine the energy level systems in superconductors before introducing SIN and SIS tunneling. There are two different representation of the energy levels associated with superconductors which are semiconductor and Boson condensation representations. Semiconductor representation suggests that at absolute zero superconductors have an energy gap $E_g = 2\Delta$ between a lower energy band which is full of superelectrons and an upper energy band which is totally empty. Above the 0 K, some of the electrons, which are often called as quasiparticles, are excited from the lower band to the upper. According to Boson condensation representation, all the Cooper pairs are condensed into a level located at a distance Δ below the bottom of the conduction band at absolute zero, so called ground state for superconductors. Above the 0 K, some of the Cooper pairs break up and quasiparticles occur. The Boson condensation representation is a little more convenient than the semiconductor representation for analysis of the tunneling of super electrons.

2.3.1. SIN Tunneling

Because of the existence of energy gap in the electron density of states of superconductors, current-voltage characteristics of Superconductor-Insulator-Normal Junction (SIN) deviate from straight line observed in NIN junctions (Giaver 1960). Figure 2.5 shows Bose-condensation representation of SIN tunneling process at absolute zero. In the unbiased case tunneling does not occur, because all the electrons within Δ of the Fermi energy have fallen into the superconducting state there are no electron states for the normal single electrons to tunnel into or out. This is also true for the range $-\Delta/e<V<+\Delta/e$ of biases. In the case of $V\geq\Delta/e$, the Fermi level of the normal metal is moved up by the value of eV above the ground state of the superconductor. Therefore electrons can tunnel from the conduction band of the normal metal to the empty states above the gap of the superconductor. For a negative bias, $V\leq-\Delta/e$, tunneling involves the breakup of a Cooper pair, with one electron of the pair tunneling down to the top of the normal metal conduction band and the other jumping upward to the quasiparticles energy band of the superconductor. Hence breaking up a pair creates a quasiparticle inside the superconductor and electrons passing through the insulating layer reach the normal metal (Poole, et al. 1995).

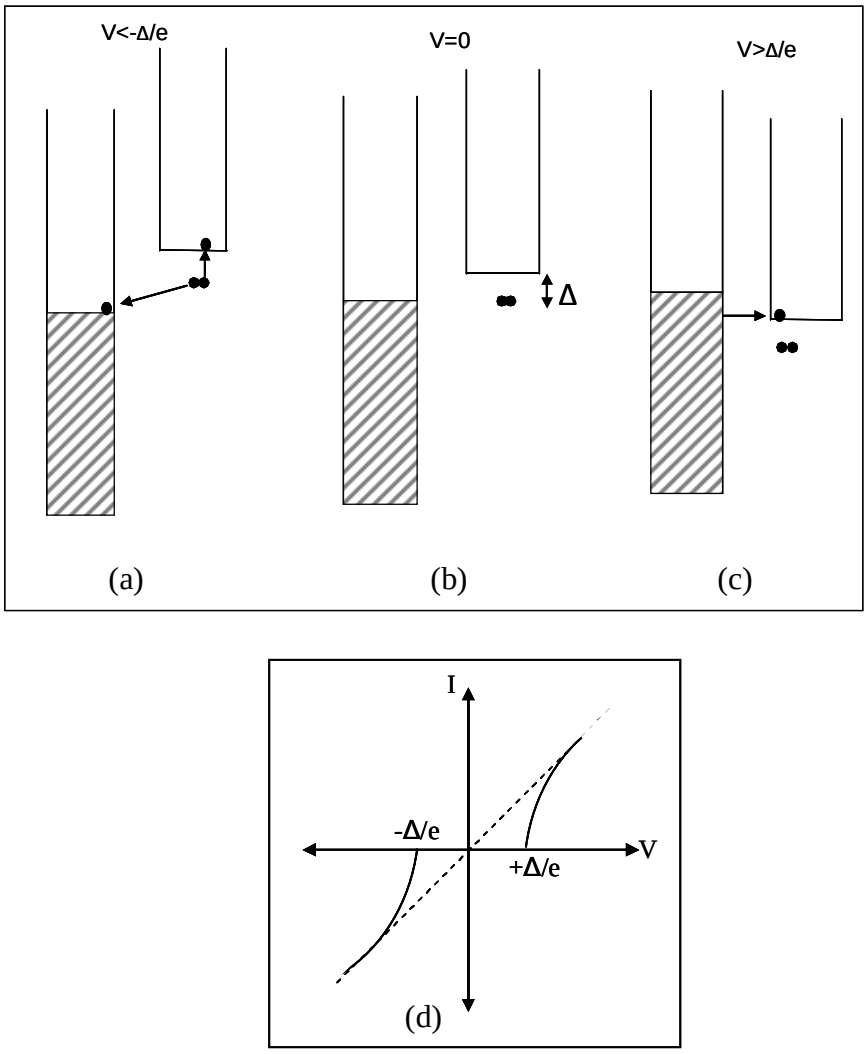

Figure 2.5. The SIN tunneling process with representation of Boson condensation and its current-voltage (I-V) characteristic at T= 0 K

The total tunneling current in an SIN junction can be determined by the independent particle approximation introduced in Equation 2.2 as,

$$I(V) = c\int |T|^2 N_n(E) N_s(E + eV)[f(E) - f(E + eV)]dE \qquad (2.3)$$

When one of the electrodes is a superconductor, the application of many-body field theory shows that the differential conductance is proportional to the density of states in the superconductor. One assumes that the normal metal electrode has a well-behaved almost constant density of states near the Fermi energy. When the gap opens up in a superconductor, the quasiparticle states are pushed to the gap edge resulting in a singularity in the density of states:

$$\frac{N_s}{N_n} = \begin{cases} 0 & |E| < \Delta \\ \dfrac{E}{\sqrt{E^2 - \Delta^2}} & |E| \geq \Delta \end{cases} \tag{2.4}$$

There are no quasiparticle states within the gap i.e. E < Δ. At low temperatures, the differential conductance directly measures the density of states:

$$G_{ns} \propto N_s(e|V|) \tag{2.5}$$

Rigorous derivation of this result requires many-body calculations. Therefore, it is surprising that this correct result can be obtained from the equation for the current in the independent particle model (Equation 2.1) by assuming a BCS density of states in the superconductor. This model was used by Giaever to explain his pioneering tunneling results on superconductors.

2.3.2. SIS Tunneling

Bose condensation representation of the S-I-S tunneling process is shown in Figure 2.6. At T=0 K, minimum voltage necessary to produce electron tunneling is V> $(\Delta_1+\Delta_2)/e$ where Δ_1 is the energy gap of the first superconductor and Δ_2 is the energy gap of the second superconductor. According to the tunneling process, a Cooper pair breaks up in the first superconductor and one of the electrons belongs to pair tunnels to the empty (quasiparticle) energy state of second superconductor. Since releasing energy from pair breaking is equal and greater than the energy gap value of first superconductor, the second electron of broken pair is excited to the quasiparticle energy state of first superconductor (Schmidt 1997). At voltage $V=-(\Delta_1+\Delta_2)/e$ direction of tunneling reversely changes. For temperature T>0 K, the tunneling current can also flow at lower voltages because of the availability of the thermally excited quasiparticles.

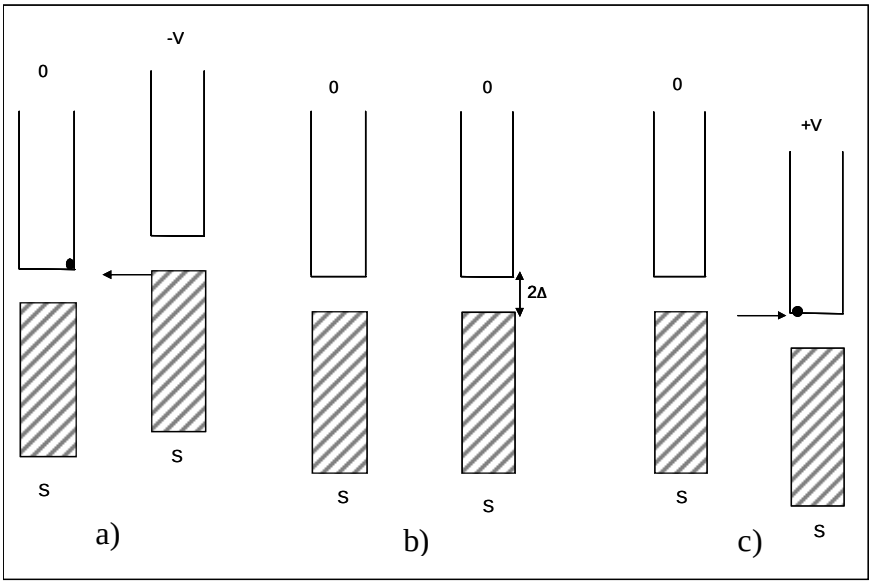

Figure 2.6. Bose condensation representation of single electron tunneling between two identical superconductors at absolute zero

The SIS tunneling current passing through the barrier is denoted as Equation 2.6.

$$I(V) = c\int |T|^2 N_{1s}(E) N_{2s}(E+eV)[f(E) - f(E+eV)]dE$$

$$= c|T|^2 N_{1n}(0) N_{2s}(0) \int \left[\frac{|E|}{\sqrt{E^2 - {\Delta_1}^2}} \frac{|E+eV|}{\sqrt{(E+eV)^2 - \Delta^2}} (f(E) - f(E+eV)) \right] dE \quad (2.6)$$

The range of the integration excludes values of E such that $|E|<\Delta_1$ and $|E+eV|<\Delta_2$.

SIS junctions differ from other junction types in that they show supercurrent tunneling due to Cooper pair transfer between two superconductors which is called Josephson current apart from the quasiparticle tunneling. The existence of the Josephson current, I_c, depends on the junction resistance and given by Ambegaokar-Baratoff theory (Ambegaokar and Baratoff 1963) for BCS superconductors,

$$I_c R_n = \frac{\pi\Delta(0)}{2e} \quad (2.6)$$

where I_c is the Josephson current, R n is the normal state resistance of the junction and $\Delta(0)$ is the energy gap at T=0 K.

Figure 2.7 shows ideal current-voltage characteristics of a Josephson junction at T=0 K for identical superconductors. The current at zero bias is direct result of the Cooper pair tunneling and is known as the Josephson current. We can apply a dc current to the junction and not develop a voltage drop across it. However, there is a limit to the amount of current that the tunneling Cooper pairs can carry. When the applied current exceeds the critical current, the lossless current transport breaks down and the system switch from a zero voltage to a finite voltage state that corresponds to the double gap energy 2Δ. This gap energy is also expressing the binding energy of the Cooper pairs. Then, the tunneling current is dominated by quasiparticles. Further increase of the current merely displays the Ohms law at $V>2\Delta/e$. While decreasing the current we observe a hysteretic behavior. The tunneling current remains to be carried by quasiparticles. For the zero temperature the current should decrease to zero before the zero voltage state would be achieved again.

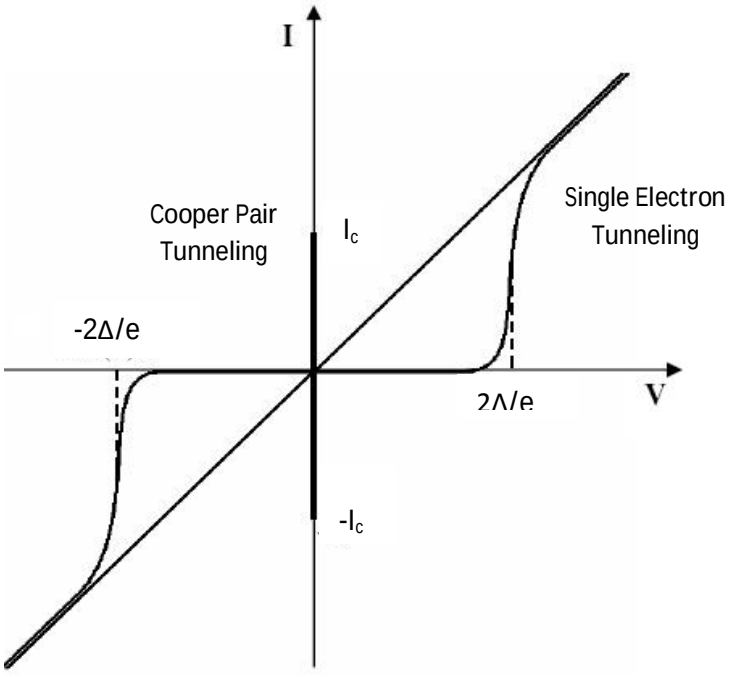

Figure 2.7. I-V characteristics of an SIS junction at T=0 K
(Source: Wesche 1998)

I-V characteristic of layered HTSs along the natural IJJ stacks includes several branches due to individual switching of each junction from Josephson state to

quasiparticle state when the bias current exceeds the individual critical current of each junction (Yurgens 2000). Thus each of the junctions acts as one of the single branch in large gap voltage of all junctions and the branches are almost vertical these voltages.

The poor thermal conductivity of Bi2212 single crystal causes a local overheating in superconductor structure. Overheating and nonequilibrium effects are the most encountered problems whilst obtaining I-V data, up to now various research groups have investigated this subject (Tanabe, et al. 1996, Yurgens, et al. 2004). As increasing the number of IJJs in the quasiparticle state, the overheating increases and causes smaller voltage jump (conductance peak) in I-V curves. Moreover Non-equilibrium effect that is easy quasiparticle self injection through the high transmissive IJJ tunneling barrier (about 0.3 nm thickness in Bi2212) increases the heating effect in the structure. This effect also leads to back-bending of the I-V curve in the sub-gap region. One of the methods to eliminate heating problem is to use stacks of intrinsic junctions (mesas) with small dimensions in order to reduce I_c (Zhu, et al. 2006). However, since the same current per unit area through the junctions flows, the non-equilibrium effect still occurs and causes the Joule heating (Zasadzinski 2002). Therefore this method is partly successful in observing the energy gap in I-V curves. One another method is to use the short current pulse tunneling measurements which provides free I-V characteristic different from gap suppression because of joule heating in IJJ (Suziki, et al. 1999). However, much of the interest of these measurements is in the behavior close to the energy gap, and high bias currents are required. Another alternative method is to intercalate the Bi2212 single crystals along the c axis with inert guest molecules such as $HgBr_2$, HgI_2 or I_2 molecules to reduce the coupling between CuO_2 layers. Due to intercalation the intrinsic tunneling barriers are becoming wider which results in a drastic decrease of the c-axis critical current density. Therefore, Joule heating can be significantly suppressed.

2.3.3. Spin Polarized Tunneling

Ferromagnet/Superconductor single tunnel junction consists in a ferromagnetic layer that is in the top and a superconducting layer that is in the bottom. Both layers are divided by a thin insulator that works as tunnel barrier. A nonequilibrium spin polarization in a superconductor can be generated by passing electrical current through

a ferromagnetic material before the tunneling across a thin insulating barrier into a superconductor. The basic principle can be understood by studying Figure 2.8, which illustrates the spin dependent density-of-states (DOS) diagrams of a ferromagnet and superconductor. The DOS at the Fermi energy for a ferromagnet is different for spin-up and spin-down electrons, as shown in the schematic, where spin up has been assumed to be the majority carrier. Cooper pairs in spin singlet superconductors are formed between up and down spins and so cannot carry a spin current. It is therefore spin-polarized electron tunneling into superconductor can be performed by applying a potential difference between the ferromagnetic material and superconductor. Since the DOS at the Fermi energy in ferromagnet is larger for electrons with spin up than for electrons with spin down, most of the electrons injected into superconductor will have spin up. This leads to spin accumulation in superconductor.

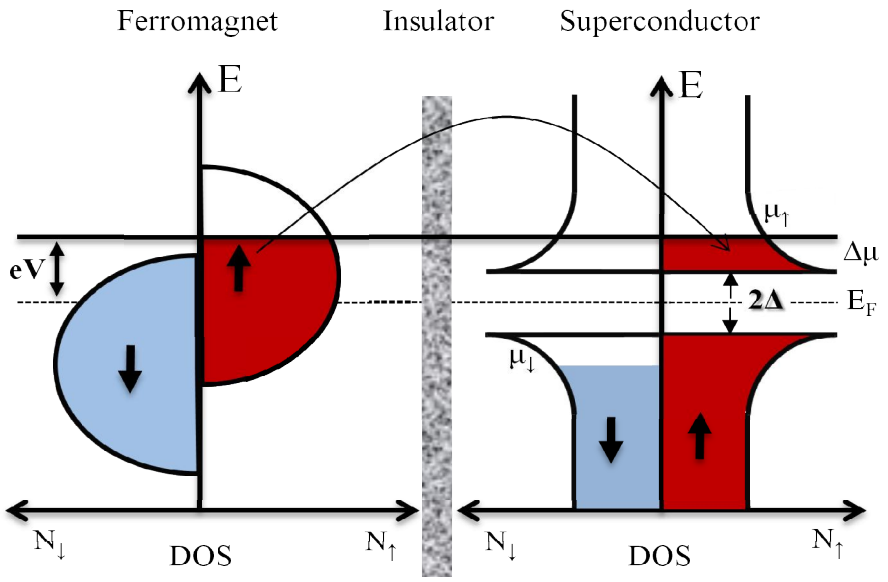

Figure 2.8. Spin dependent density-of-states (DOS) diagrams of a ferromagnet and superconductor

To preserve charge neutrality in each of the metals, an increase in the number of electrons with spin up is accompanied by a decrease in the number of electrons with spin down. Therefore charge transport across the F-N interface is accompanied by spin transport. This produces the nonequilibrium configuration of the chemical potentials. $\mu N_\uparrow$ increases with respect to its equilibrium value and due to charge neutrality $\mu N_\downarrow$ has to decrease so that the total DOS at any position in N is uniform. Since in N the DOS is

spin independent, the size of the increase in $\mu N_{\uparrow}$ is equivalent to the size of the decrease in $\mu N_{\downarrow}$. The chemical potentials of the spin-up and spin-down electrons are shifted oppositely by μ from the equilibrium to produce the nonequilibrium spin density.

As mentioned above the high density of spin injection through a tunneling barrier induces a spin imbalance. Therefore, not all electrons of one spin species are able to find a corresponding electron of the opposite spin species in order to form Cooper pair. The injection of spin-polarized quasiparticles is expected to enhance the nonequilibrium because the spin-relaxation time is estimated to be much longer than the quasiparticle-recombination time. This nonequilibrium state results in a suppression of superconductivity. Two primary effects on the suppression of superconductivity can be considered (Schmid and Schon 1975). One is associated with the resulting excess magnetic moments that break the time-reversal symmetry in singlet superconductors. The other is the excess momentum and the nonequilibrium quasiparticle distribution that modify the energy spectrum of the superconductor (Tinkham 1996, Gray 1981).

2.4. THz Waves Generation from $Bi_2Sr_2CaCu_2O_{8+\delta}$

The ac Josephson effect allows for the construction of voltage to frequency converters that have great potential for the THz frequency range. The ac Josephson effect arises when a voltage bias is established across a Josephson junction. An ac-current appears that oscillates at the Josephson frequency $f_J = V/\Phi_0$. V is the voltage across the junction and Φ_0 is flux quantum. According to this equation, 1 mV corresponds to an emission frequency of 0.483 THz for a single junction. Thus Josephson junctions and arrays of Josephson junctions are potential sources of high-frequency electromagnetic radiation.

Radiation from a Josephson junction directly in the microwave frequency range has been detected a long time ago (Langenberg, et al. 1965). However, radiation power is limited to the pW range (Langenberg, et al. 1965) and it is too small for practical applications. Since a significant effort has been devoted to develop JJ arrays as coherent sources of radiation (Jain et al. 1984, Lukens 1990, Barbara, et al. 1999). A major challenge is to force all JJs in array to emit coherently, so that total emitted power increases proportionally to the square of the total number of junctions in the array (Jain, et al. 1984). Artificial junctions always have slightly different junction parameters,

especially the Josephson critical current. This leads to desynchronization and dramatic drop in emission power. Therefore, the major challenge is to synchronize Josephson oscillations in all junctions. Also, as the maximum frequency is limited by the superconducting gap, it cannot exceed several hundred gigahertz for structures fabricated out of conventional superconductors.

Demonstration of intrinsic Josephson effect in layered high temperature superconductors (Kleiner, et al. 1992), such as $Bi_2Sr_2CaCu_2O_{8+d}$ (Bi2212), opened a completely new route to developing electromagnetic sources. Large values of superconducting gap up to 60 meV allow bringing the Josephson frequency into the practically important terahertz range. Moreover, intrinsic JJs (IJJs) have much closer parameters than artificial ones as these parameters are controlled by the atomic crystal structure rather than by amorphous dielectric layer in artificial JJs. Also, layered superconductors provide a very high density of IJJs (1 per 1.56 nm along the c-axis) and thus it is easy to reach super-radiation regime with many junctions on the scale of radiation wave length. There have been many attempts to obtain THz radiation from layered superconductors using IJJ properties. Nevertheless, the same challenge to synchronize oscillations in all junctions also remains for this system.

High-frequency emission of unsynchronized intrinsic junctions has been observed up to 0.5 THz from Bi2212 with a weak power (Batov, et al. 2006). Numerous approaches for synchronizing the junctions have been considered, such as applying a magnetic field to induce coherent Josephson vortex flow (Irie, et al. 1998), inserting the Bi2212 crystal into a microwave cavity (Madsen, et al. 2004), the use of shunting elements in parallel to small sized stacks (Wang, et al. 2000), the excitation of Josephson plasma oscillations via heavy quasiparticle injection (Kume, et al 1999) or the investigation of stimulated emission due to quantum cascade processes (Krasnov 2006). The strategy perhaps investigated most intensively considered the generation of collective Josephson oscillations by a lattice of moving Josephson vortices, exciting electromagnetic cavity resonances inside the stack (Kadowaki, et al. 2006, Bae, et al. 2007) in order to generate noticeable radiation oscillations induced by the moving lattice have to be in phase in different layers, which is realized only if the moving vortices form a rectangular lattice. However, such a rectangular lattice is usually unstable in most of parameter space (Koshelev and Aranson 2001). In other words, the vortex–vortex interaction favors the triangular lattice that can produce only weak noncoherent radiation.

L. N. Bulaevskii and A. E. Koshelev proposed that mesa with small lateral size and a very large number of junctions (about 10^4) in zero magnetic field can provide high radiation power and efficiency in the THz frequency range (Bulaevskii and Koshelev 2007). They show that in such a design oscillations in different junctions are synchronized by the external electromagnetic radiation field generated by the oscillations them-selves (Bulaevskii and Koshelev 2007). Fabrication of a mesa with such a large number of almost identical junctions is technological challenge of this design.

An experimental breakthrough was achieved in 2007. Ozyuzer et al. succeeded in generating intense, coherent, continuous and monochromatic electromagnetic waves in the THz frequency region emitted from rectangular mesa structures of intrinsic Josephson junctions (IJJ) in $Bi_2Sr_2CaCu_2O_{8+d}$ (Bi2212) . The fundamental frequencies of the observed emission were as high as 0.85 THz and radiation power was up to 0.5 μW. In contrast to previous studies, the radiation was detected outside the cryostat after traveling through ambient space. This is only possible since the power emitted from this device is several orders of magnitude stronger than the previous ones. Another striking contrast to the previous results is that emission does not require the application of a magnetic field, considerably simplifying the design of superconducting THz sources. In fact, a single applied dc current leads to the efficient excitation of continuous coherent THz radiation.

In this work, the Bi2212 mesas were designed as electromagnetic resonator-cavities. The dimensions of the mesas are 300 μm in length, 40-100 μm in width, and about 1 μm in height. A Schematic layout of the Bi2212 mesas is shown in Figure 2.9. When an external current is applied along the c axis, the ac Josephson current in the resistive state excites a cavity resonance mode of Josephson plasma wave in the sample. The excited standing wave of Josephson plasma is converted to a terahertz electromagnetic wave (em) at the mesa surfaces and the em wave is emitted into the vacuum space of the mesa.

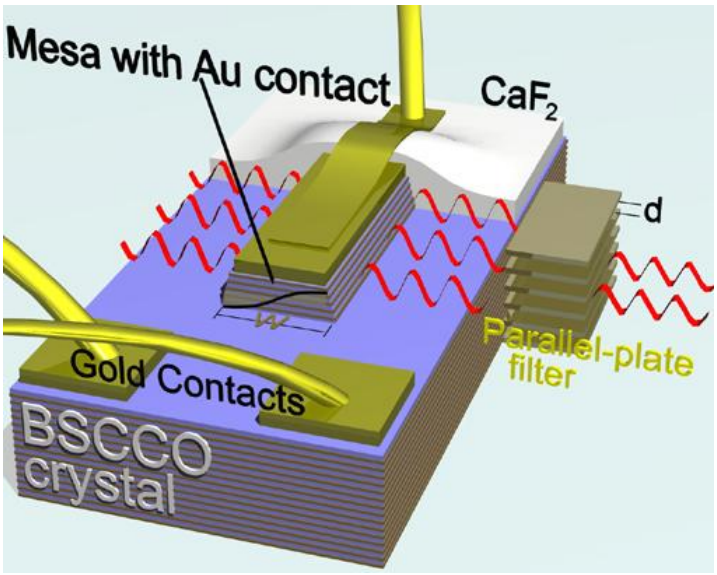

Figure 2.9. Schematic of mesa and electrical contacts on Bi2212 for emission of THz radiation (Source: Ozyuzer, et al. 2007)

The operation of the THz-source is based on the propagation of electromagnetic waves inside the layered Bi2212 structure as Josephson plasma modes (Kleiner, et al. 1994). The mode with the highest velocity is the in-phase mode in which all junctions oscillate in-phase and the mode with the lowest velocity is the anti-phase mode in which neighboring junctions oscillate out-of-phase (Figure 2.10.a and Figure 2.10.b). Only the in-phase mode produces noticeable emission because the average electric field on the side surfaces cancels in other modes. In the in-phase mode, the coherent superposition of the electromagnetic waves from each junction creates a macroscopic coherent state in which the radiation power increases as the square of the number of junctions. In mesas with lateral dimensions that are smaller than the propagation distance of the Josephson plasma modes, multiple reflections at the side faces of the mesa create a standing wave pattern and Fabry-Perot type cavity resonances, or Fiske resonances. A resonance condition occurs whenever the Josephson frequency, $f_{Jos=} V/(N\Phi_0)$, equals the cavity frequency, $f_{cav} = c_0/2nw$. Here, w is the width of the cavity, V is the voltage applied across the junction stack, Φ_0 is magnetic flux quantum, and N is the number of active junctions in the stack. As the resonance condition is approached, for example by scanning the applied voltage, energy is pumped into the cavity resonance. As the cavity field builds up it entrains the oscillations of more junctions leading to a further increase of the cavity field until (almost) all the junctions are synchronized into a coherent in-phase oscillation accompanied by a large cavity field. This process resembles the

emergence of coherence in a laser cavity. Furthermore, the resonance condition implies that the emission frequency can be controlled by the mesa width according to f~1/w.

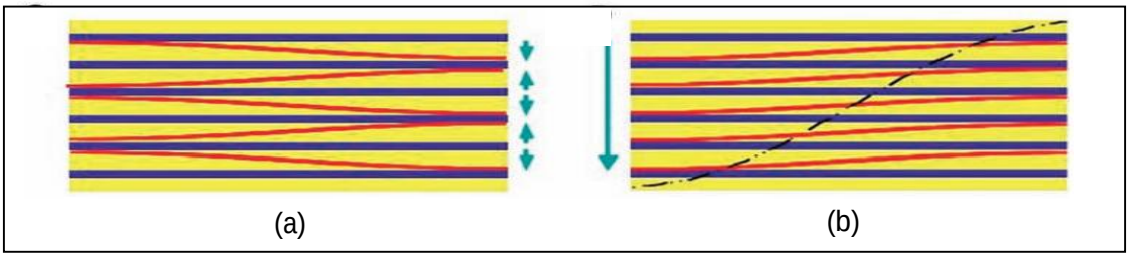

Figure 2.10. Schematics of the anti-phase (a) and of the in-phase (b) mode (Source: Ozyuzer, et al. 2007)

These studies stimulated further work on THz generation from intrinsic Josephson junctions in Bi2212 mesas and recently one order of magnitude larger radiation power (5 μW) and higher harmonics (up to fourth order, corresponding to 2.5 THz) have been obtained (Kadowaki, et al. 2008). Tunability of the THz emission and local temperature properties have also been studied (Gray, et al. 2009, Kurter, et al. 2009, Wang, et al 2009). Using low temperature scanning laser microscopy, Wang, et al. 2009 imaged electric field distributions in the junction stack of $Bi_2Sr_2CaCu_2O_{8+d}$. They observed standing electromagnetic waves (cavity resonances), thus provided a direct confirmation of cavity modes observed in the previous experiments. In high bias region where the I-V curve is back bending, the authors observed that hot spots with temperature higher than T_c are created, and their positions vary with the external current. It is argued that these hot spots can be used to tune the cavity size, and thus the radiation frequency (Wang, et al. 2009).

Many theoretical models have been proposed to explain the IJJ effect and the mechanism of THz wave generation from Bi2212 mesas. One model is based on the modulation of the Josephson critical current density along the width of the mesa, which allows for the efficient excitation of the cavity resonance under zero magnetic fields (Koshelev and Bulaevskii 2008). In another model (Lin and Hu 2008, Koshelev 2008), a new dynamic state has been discovered in which a phase kink occurs, enabling the excitation of the resonance. A recent suggestion is that the nonradiative component of the oscillating magnetic field of the cavity resonance mode determines the THz emission (Tachiki, et al. 2009). However, details of the mechanism have not yet been clarified.

CHAPTER 3

EXPERIMENTAL

3.1. Motivation

Recently, it has been demonstrated that rectangular IJJ mesa structures of Bi2212 can be used as a source of continuous, coherent and polarized THz radiation. All THz emitting mesas are below a certain underdoped level, which has relatively small critical current in contrast to optimally doped and overdoped Bi2212. In this work our aim is to decrease the critical current density of as grown Bi2212 single crystals using spin polarized current and eliminate the adjustment of doping level for successful THz emission. For this aim, rectangular Au/Co/Au/Bi2212 mesa structures with large areas and high thicknesses were fabricated by various experimental processes. In order to characterize the Bi2212 mesas, c-axis resistance versus temperature (R-T) and current-voltage (I-V) tunneling characteristics were investigated. During I-V characterization, we used a Si composite bolometer to detect the THz emission. In this chapter, all of experimental processes will be described step by step.

3.2. Mesa Fabrication

In this work, experiments were performed on as-grown Bi2212 single crystals which were grown using floating zone method by Huabing Wang at National Institute for Materials Science, Japan. In order to form Au/Co/Au/Bi2212 mesa structures on the smooth surface of as-grown Bi2212 single crystals, many experimental processes were used. First of all, single crystal of Bi2212 was glued onto a sapphire substrate from its smooth a-b surface by silver epoxy (Figure 3.1.a). In order to get fresh and smooth surface on Bi2212, the crystal was then cleaved with a scotch tape (Figure 3.1.b). After that, Au layer with the thickness of 8 nm was immediately deposited on the cleaved crystal surface using thermal evaporation technique to prevent the chemical reactions between Co layer and Bi2212 crystal (Figure 3.1.c). Increasing thickness of the Au

layer causes the reduction of spin polarization of the quasiparticles (Ishibashi, et al. 2001) so thin Au layer was used to keep polarization of spins.

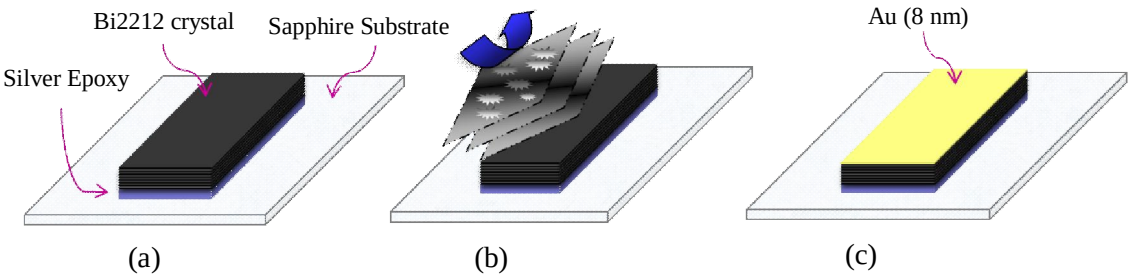

Figure 3.1. Schematics of (a) Adhesion of the crystal on substrate (b) Cleaving the crystal (c) Gold layer on the cleaved crystal surface

Schematic representation of our thermal evaporation system can be seen in the Figure 3.2. Thermal evaporation technique is fast and comparatively simple; it registers a low-energy impact on the Bi2212 surface; that is, no surface damage results. This technique includes evaporation of the material in filament boat heated by high current source and re-condensation of the heated material with vapor state onto cooler substrate in a vacuum. Generally it needs high temperatures to evaporate the material and in our system it is carried out by passing large current through the filament boat. The value of the current necessary for evaporation temperature changes with respect to filament boat resistance (its sizes). It is between 190 and 200 A for our filament boat. For the good quality film evaporation should be done in vacuum around 10^{-6} Torr. It is not only necessary to avoid reaction between the vapor and atmosphere but also to increase the mean free path of vapor atoms. Thus they do not undergo collisions with the surrounding gas molecules inside the evaporation chamber. In order to reach high vacuum, turbo molecular pump with back pumping was used in our system. Deposition and thickness of the film on the substrate were controlled by shutter and it also provides to get good quality thin films which have not contamination coming from other materials in the boat at the starting of evaporation. Thickness of the deposition was measured by thickness monitor and shutter was closed when required thickness was reached.

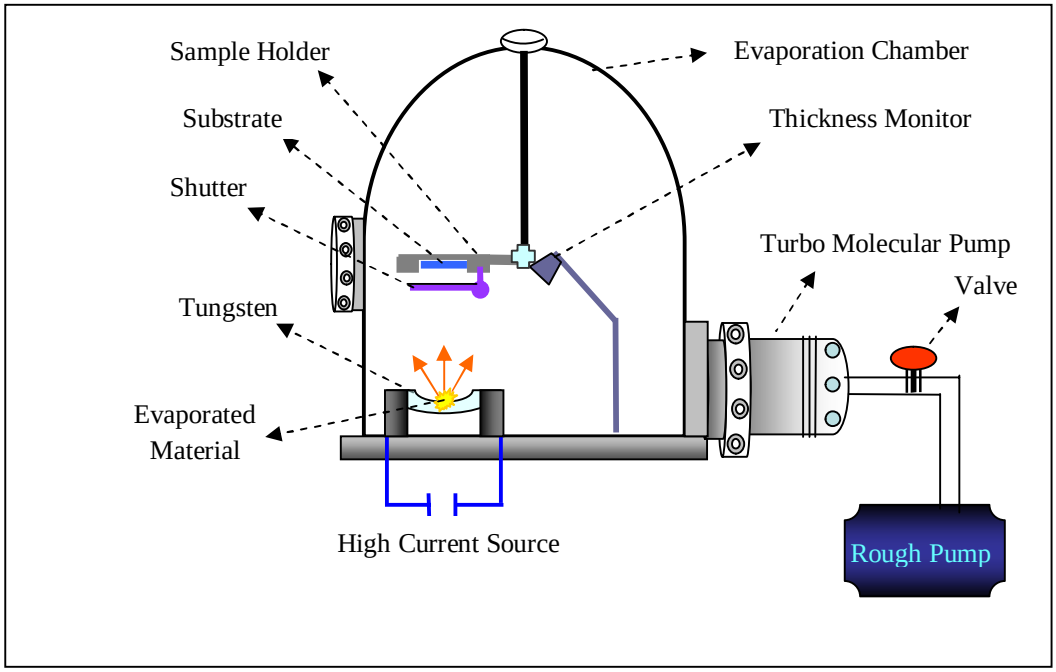

Figure 3.2. Schematic of our thermal evaporation system

After the 8 nm Au evaporation, 60 nm Co layer was deposited on thin Au layer as a spin injector (Figure 3.3.a) and then in order to prevent oxidation 100 nm thick Au layer was deposited on the top of Co layer (Figure 3.3.b) using DC magnetron sputtering process . The final side view of the Au/Co/Au/Bi2212 multilayer is seen in the Figure 3.3.c.

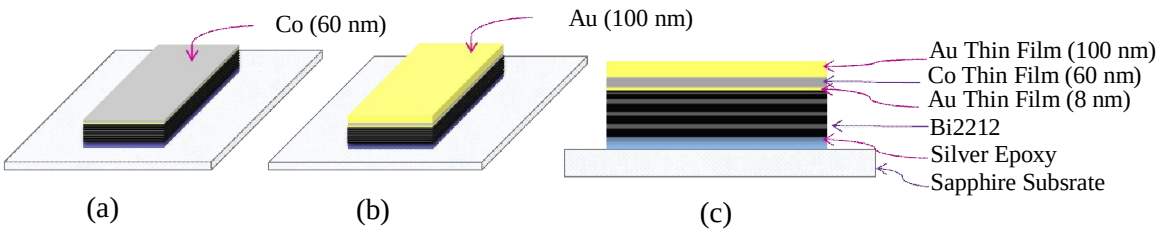

Figure 3.3. Schematics of (a) Co layer on thin gold layer, (b) Gold layer on top of Co layer and (c) final side view of the Au/Co/Au/Bi2212 multilayer

Sputtering in its many forms has become perhaps the most widespread used physical vapor deposition process. When a solid surface is bombarded with energetic particles such as accelerated ions, surface atoms of the solids are scattered backward due to the collisions between the surface atoms and the energetic particles. These atoms then bond at the atomic level to a substrate and create a thin film. This phenomenon is called sputtering. Several types of sputtering processes exist, including: ion beam,

diode, and magnetron sputtering. The main difference between magnetron sputtering and other sputtering methods is the application of magnetic field around the sputtering target in order to energize argon atoms for bombarding the target. Using magnetic field leads to trapping electrons in the magnetic field created around the target which enhances plasma. This results in higher ionization of Argon atoms and bombarding rate that finally increases deposition rate.

Magnetron sputtering system that is used in our experiments is a High-Vacuum system shown in Figure 3.4. This system has 4 guns with a water cooling channel, gas entrance and power connections. A rough pump and a turbo molecular pump (TMP) were used to reach high vacuum region (below 2.0×10^{-6} Torr). A gate valve with a stepper motor was connected to the system in front of TMP. To measure base pressure of the system, a thermocouple and a cold cathode gauge were used. After reached to base pressure, Argon gas (purity 99.99%) was flowed to the chamber using a mass flow controller. The dc voltage was exploited to produce and to sustain plasma inside the chamber. To measure pressure of the vacuum chamber during the deposition, Baratron was used. The Figure 3.5 represents schematic of DC magnetron sputtering system in our laboratory.

Depositions were done in two steps. Firstly, pre-sputtering step was performed to remove the contamination of the surfaces of Co and Au targets. In this process, the shutters of the magnetron sputter heads were closed for 5 minutes. Then, shutters were opened and the deposition of Co and Au films on to the sample continues 11 minutes for the 60 nm Co deposition and 4 minutes for the 100 nm Au deposition, respectively. The deposition parameters are shown in the Table 3.1. Substrate distance from the target surface was constant for all experiments. After deposition steps, the pressure of the chamber was reached to atmosphere pressure to remove the substrate holder from the chamber.

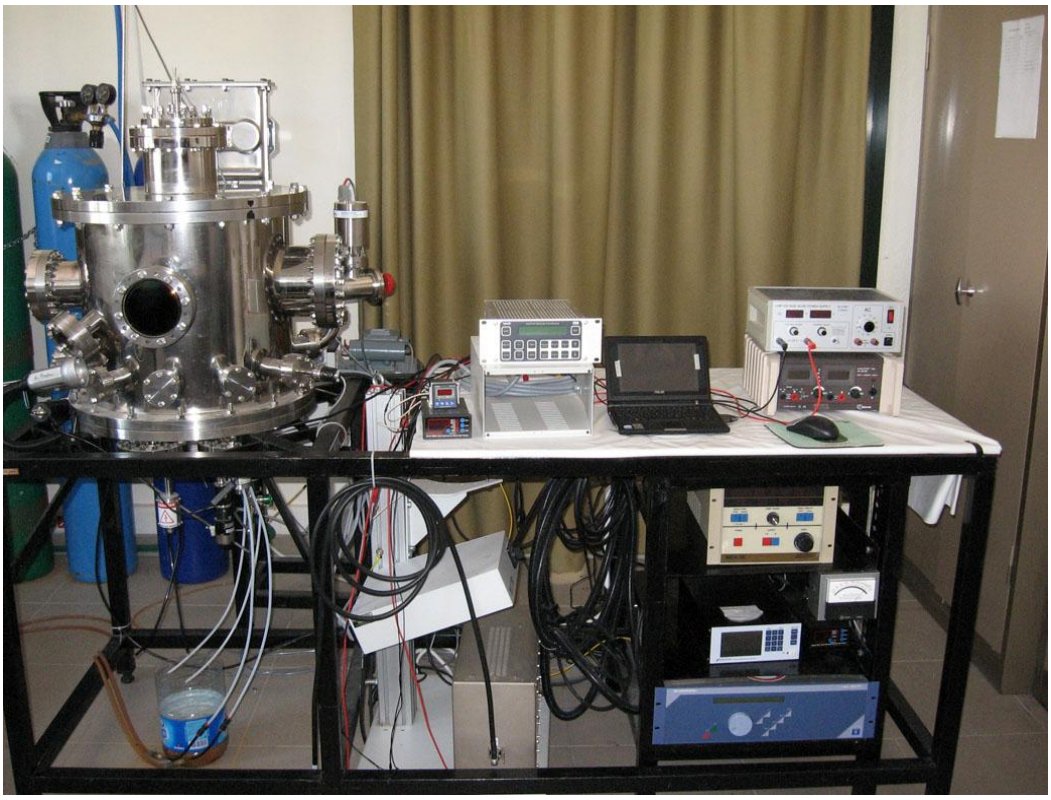

Figure 3.4. Picture of our magnetron sputtering system

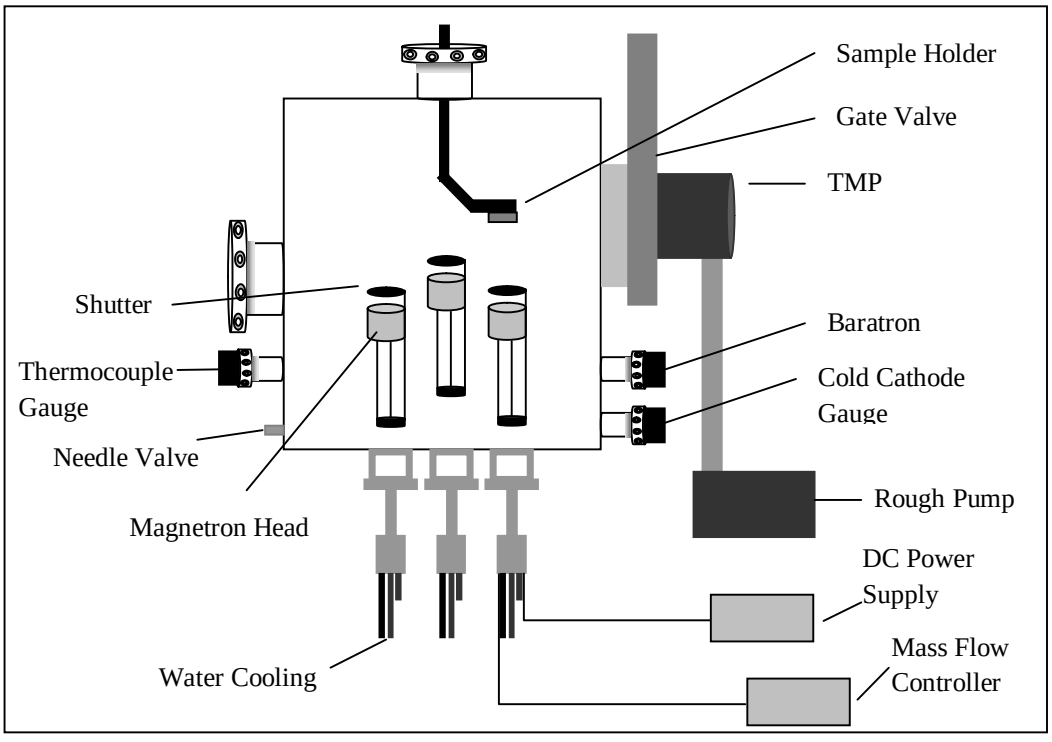

Figure 3.5. Schematic of our Magnetron Sputtering System

Table 3.1. Au and Co deposition parameters

	Au deposition parameters	**Co deposition parameters**
Power Supply	20W – 394 V – 46 mA	20W – 365V – 50 mA
Gas Flow	30 sccm Ar	20 sccm Ar
Baratron	2.96 mTorr	1.68 mTorr
Valve Position	60% Open	100% Open
Deposition Time	4 minutes	11 minutes

After the 100 nm Au deposition, the next step in the mesa fabrication is patterning the mesa shape photoresist (PR) by standard optical photolithography process. In the following, the process is described more in details, with reference to Figure 3.6 which shows an optical photolithography scheme.

Firstly, the crystal surface was covered with PR by spin coater. The spinner was rotated at 4.5 V by using power supply for 25 s giving a 1.5 µm layer of resist. The spin coating step was ended with a thermal treatment of the sample in an oven at 90°C for 30 minutes in order to drive off the excess solvent of the PR solution. For the third step, the exposure, a mesa shaped mask was placed between UV source and the sample. The resist is a sensitive solution which changes its chemical properties if exposed to a suitable radiation; in particular resist solubility is modified in an appropriate solution called developer which was sodium hydroxide (NaOH) with concentration of 0.2 M in our case. According to the desired pattern, some adsorbing and transparent regions are present on the glass mask; as a consequence only some regions of the sample are exposed by UV radiation. Therefore, during the exposure, the solubility of the resist was changed only near the incident radiation, that is to say that only the exposed areas were chemically modified. Afterwards, in the development step, only the exposed resist was removed, thus producing a resist pattern that was a replication of the mask pattern. The sample was then rinsed in distilled water and dried with flow of N_2. Finally, the mesa shaped patterned samples were exposed UV light for 10 seconds for the blanket exposure and hard baked at the 115°C in the drying oven for 40 minutes, which solidifies the remaining PR to make more durable layer for the reactive ion beam etching.

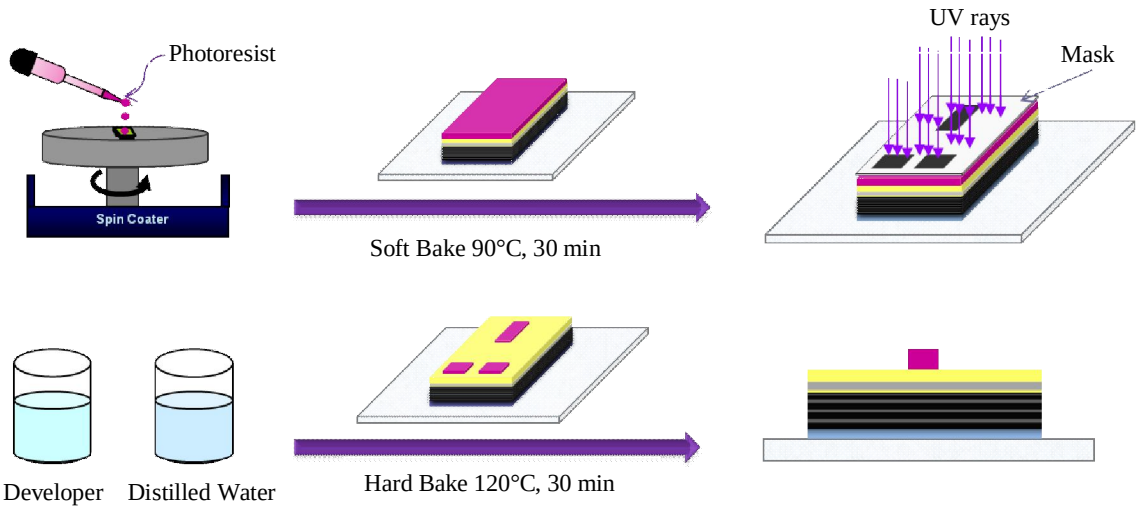

Figure 3.6. Schematic representation of photolithographic processes

After the preparation of mesa shape photoresist pattern on 100 nm gold layer, sample was mounted in ion beam etching system that produces ion beam accelerated through the surface of the sample to etch down area unprotected by PR layer on crystal. Since the regions protected by PR layer are not etched, the mesa structure with required sizes on Bi2212 single crystal is obtained after the etching (Figure 3.7).

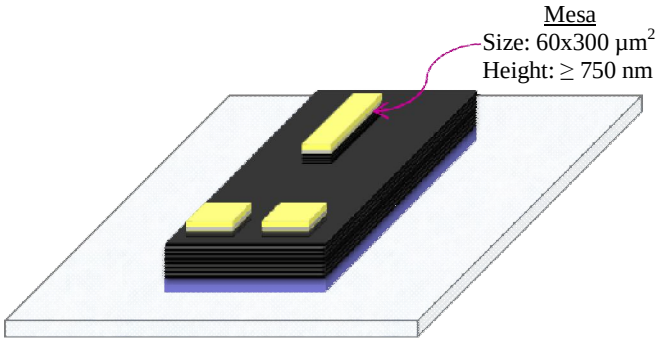

Figure 3.7. Schematic of the mesa structure

The picture and top view schematic of our ion beam etching system is shown in Figure 3.8 and 3.9, respectively. Samples were mounted to the sample holder and sample holder was placed into chamber with an angle of 67.5° with the direction of ion beam. High vacuum is necessary to increase mean free path of ion beam and it increases the possibility of etching on crystal without lost of their energies by colliding with each other and other atoms in the chamber. Therefore turbo molecular pump with back pump was used to reach the high vacuum that is 10^{-6} Torr for our system. After reached to base pressure, Argon gas was flowed to the chamber using a mass flow controller. Then,

dc voltage was exploited to produce and to sustain plasma inside the chamber; the ions beam formed in the plasma are accelerated towards the sample. The parameters for Ar ion beam etching can be seen in Table 3.2. During the etching, our sample holder was rotated with the rotary feed through to prevent the differences in lateral angles of mesa and obtain smooth rectangular mesa shape. Because of the collisions between ions and crystal atoms, heating occurs during the ion beam etching. Therefore sample holder was cooled to prevent the heating on sample during the etching by liquid N_2.

Figure 3.8. Picture of our ion beam etching system

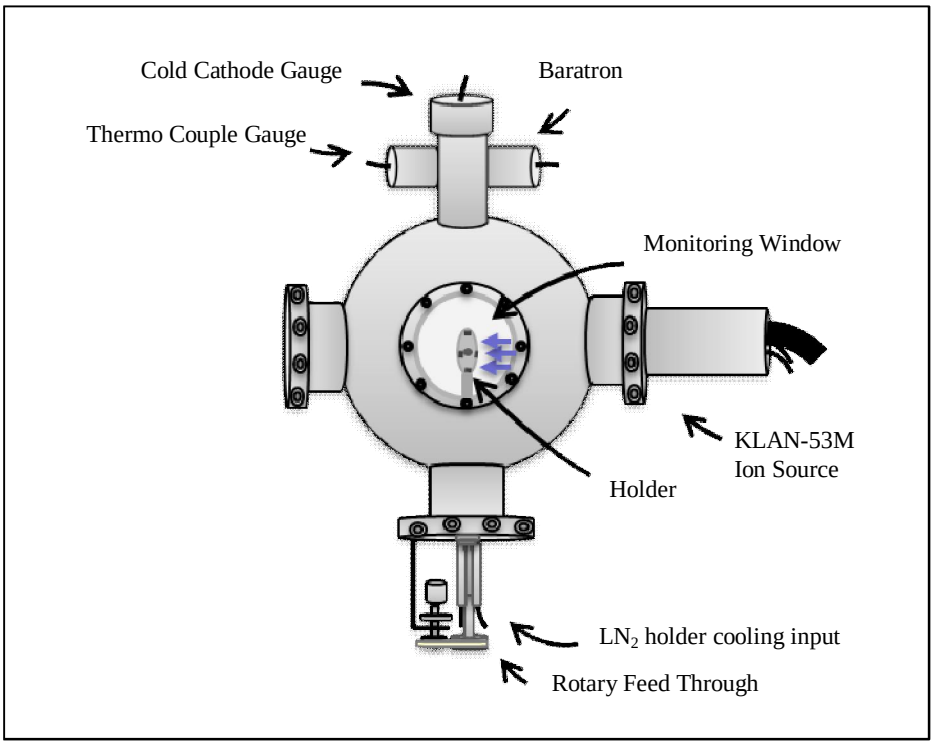

Figure 3.9. Top view schematic of our ion beam etching system

Table 3.2. Ion beam etching parameters for Ar

	Parameters for Ar etching
Discharge	50 V – 0.7 A
Cathode	320 V – 0.45 A
Acceleration	400 V – 1 mA
Ion Beam	300 V – 38 mA
Neutralizer	13 A – 38 mA
Gas Flow	2.7 sccm Ar
Cold Cathode Gauge	5 x10^{-4} Torr

Because of the difficulties in making a contact on small area of the mesa, firstly CaF_2 insulating layer was deposited by evaporation onto crystal and small area of the mesa (Figure 3.10.a). After that, a gold stripe with the width of 30 µm was created by lift-off technique on the mesa and CaF_2 layer (Figure 3.10.b). Finally three gold probe wires were connected to the two contact paths and mesa by silver epoxy. The final measurement configuration of mesa structure can be seen in the Figure 3.11.

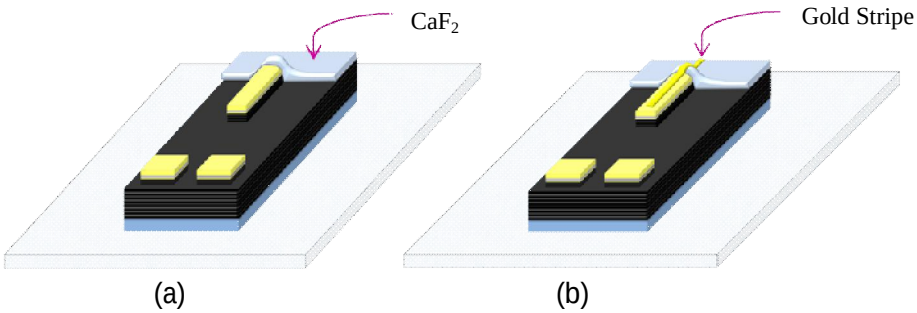

Figure 3.10. (a) CaF_2 deposition onto crystal and small part of mesa (b) Gold stripe deposition on mesa and CaF_2 layer

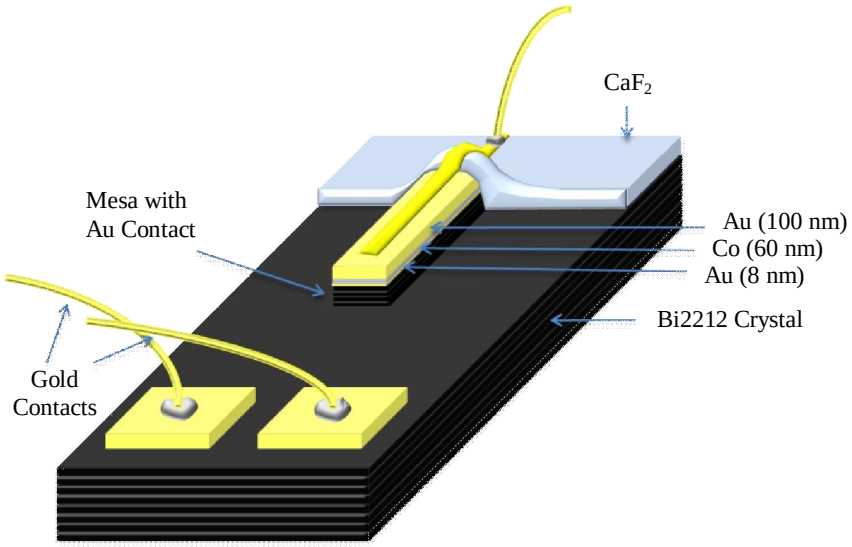

Figure 3.11. The final measurement configuration of mesa structure

3.3. R-T, I-V and Bolometer Measurements

In order to characterize the Bi2212 mesas, c-axis resistance versus temperature (R-T), and current-voltage behavior (I-V) were measured in a He flow cryostat system equipped with an optical window as shown in Figure 3.12. For cooling the crystal, liquid He was transferred from external reservoir to copper cold finger inside cryostat. The sample temperature on cold finger was controlled by heater and temperature sensor that are interfaced by a temperature controller. The system has turbo molecular pumping system that pumps between cold finger and shield of the cryostat until high vacuum. Due to the good thermal isolation, temperature of sample can be decreased up to 4.2 K and also the influence of ambient temperature on measurement is reduced by high vacuum thermal isolation.

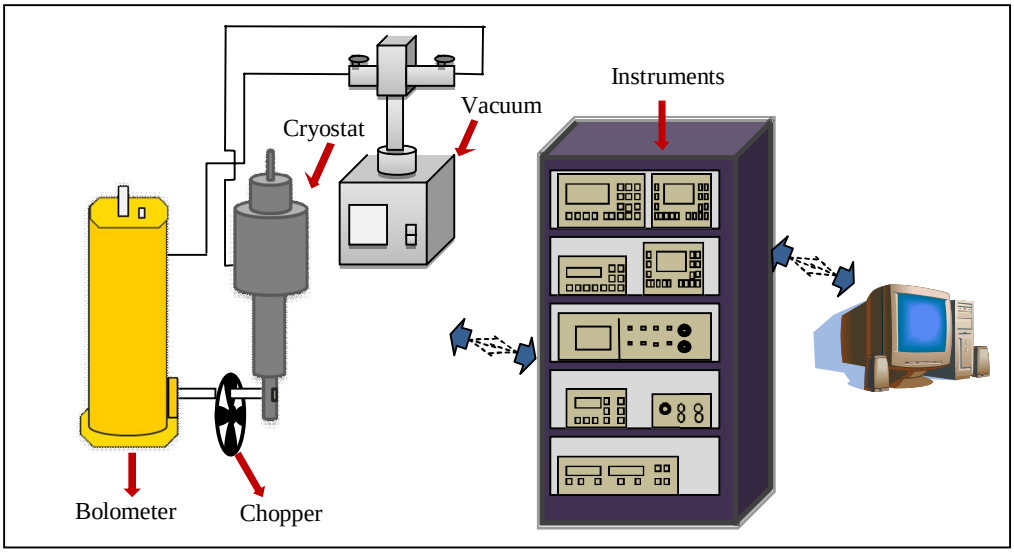

Figure 3.12. The schematic of our He flow cryostat system

The schematic representation of our experimental setups for the R-T and I-V measurements is shown in Figure 3.13. The setups are interfaced with a computer and controlled by Labview program that contains serial instrument control, data analysis and data storage. In addition its graphical programming tool provides to see the experimental result during the measurement and it has a block diagram form that allows creating program for the measurements.

During the variations of temperature from room temperature to 20 K, simultaneously changing mesa resistance values with temperature were measured using the experimental setup seen in the Figure 3.13.a. It includes current source, voltmeter and temperature controller which are interfaced with a computer. The variations at voltage and temperature were measured by voltmeter and temperature controller respectively. Since applied current along to mesa height was constant during the measurement, experimental data was analyzed and stored such as R-T by Labview program. In order to acquire accurate data, current with both positive and negative direction were rapidly applied by current source, resistance was measured twice for both direction of applied current and average of these resistances were used. Since a good thermal isolation with vacuum between cold head and shield at cryostat cannot be well created, there is a problem in thermal equilibrium between crystal and cooling head. Therefore for the accurate data, measurement during the increasing temperature is considered for R-T.

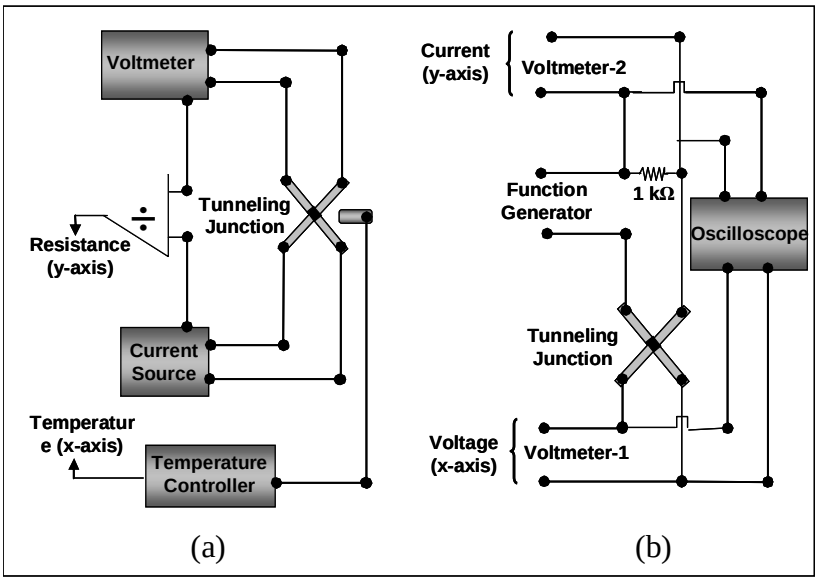

Figure 3.13. Schematic representations of (a) R-T (b) I-V measurement setups

Figure 3.13.b shows I-V experimental setup interfaced with a computer. This setup includes two voltmeters to measure voltage of mesa including all junctions and applied current on resistance serially connected to circuit between function generator and mesa. Function generator was used to apply current with required frequencies and amplitudes. Sample temperature was kept constant by temperature controller during the I-V measurement. In order to take a good I-V measurement with hysterical behavior and much quasiparticle branches, current with low frequency (5 mHz) was applied while its amplitude is gradually increasing until obtaining whole hysterical curve including normal state. Oscillator provides to see the voltage jump value and I-V before starting to measurement. Thus data including current versus voltage and constant temperature was obtained by Labview program. I-V measurements were done at various temperatures.

During I-V characterization, we used a Si composite bolometer to detect the emission power (Figure 3.12). As the applied current through the IJJs stacks was slowly swept by a function generator, the emission power from the long side of the mesa was simultaneously monitored by the Si composite bolometer. Because our Si bolometer is able to detect the discontinuous radiation, chopper between cryostat window and bolometer was mounted to modulate emission of radiation to pulse. The chopping frequency for our measurements was 70 Hz. The Si Bolometer was cooled by liquid He for its operation temperature. Output signal from bolometer was detected by lock-in amplifier and it refers to emission power of radiation emitted from mesa.

CHAPTER 4

RESULTS AND DISCUSSION

This chapter begins with electrical characterization consequences of Au /Co /Au Bi2212 mesa structures and this is followed by analysis and discussion of THz emission.

4.1. SEM and Profilometer Results

It has already been shown that the THz emission is due to a geometric resonance, e.g., it depends on the width of the mesa (Ozyuzer, et al. 2007). This assures that the sides of mesas are important because the impedance mismatch between Bi2212 and vacuum might affect the electromagnetic wave released from the mesa. In this work, surface profilometer was used to measure thicknesses of deposited thin films (Au/Co/Au) onto the Bi2212 single crystal surface and thickness of the Au/Co/Au/Bi2212 mesa structures. We employ SEM to image roughness of the side faces of the mesa. Accuracy of profilometer is just for height (c-axis) measurements, so, slope of the long side faces characterized using both SEM and profilometer images.

The step-height analyses of two fabricated mesas are shown in Figure 4.1 which belongs to FT06 and FT13. These heights include also thicknesses of deposited thin films. The height of the single crystal into the mesa can be obtained subtracting thicknesses of deposited thin films from the height of entire mesa. In order to determine the height of evaporated Au layer on the crystal surface, before starting evaporation, a piece of lamella was mounted to the sample holder near the sample. Since same gold layer thickness onto both crystal and lamella were deposited at the end of evaporation, we measured gold layer thickness on ditch in which lightly scratching only gold layer by needle. To determine the height of sputtered Co and Au layers, sputtering rates were calibrated before fabrication process. Thicknesses of deposited thin films (Au/Co/Au) and two different edges of mesa are shown in Table 4.1. In order to reach IJJ number, height of the single crystal into the mesa divided by one SIS junction size in the unit cell

which is around 1.5 nm. For example, mesa with the height of 1μm contains approximately 670 IJJs.

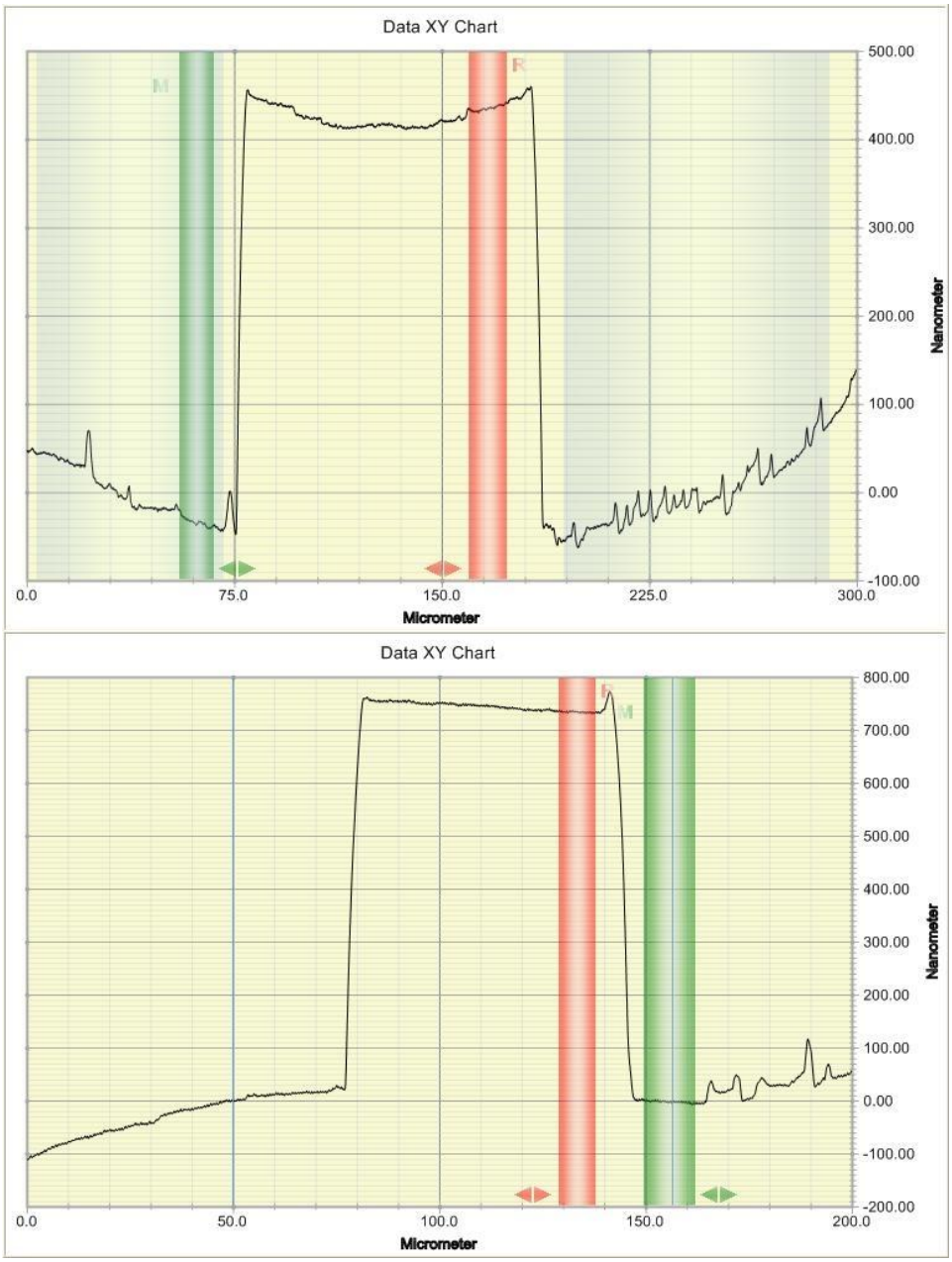

Figure 4.1. Step-height analyses of FT06 and FT13

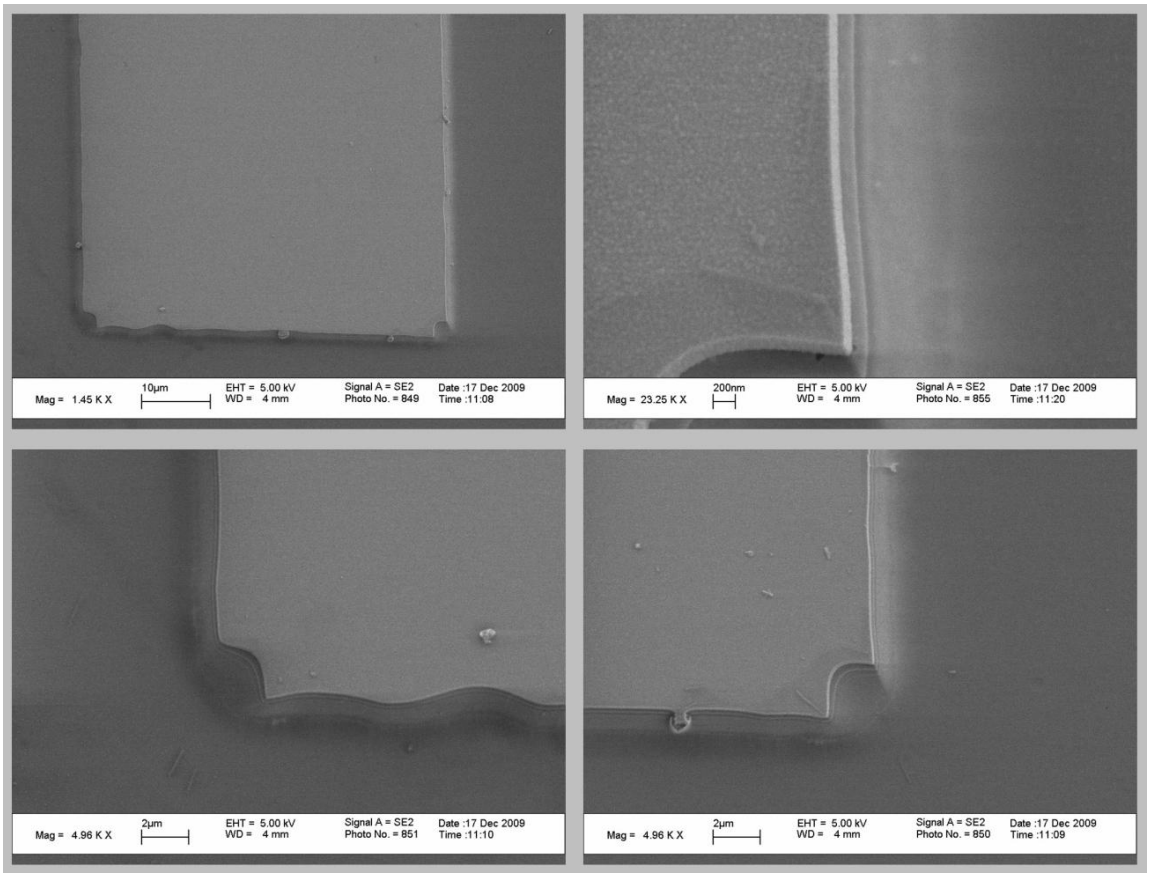

Figure 4.2. SEM images of FT34 with different magnifications

Figure 4.2 shows the SEM images of FT34 with different magnifications. It displays a considerable surface roughness of the side faces of the mesa. SEM images of the mesas indicate that mesas are trapezoidal (narrow top, wide bottom). We can find the length difference between bottom and top of one edge of the mesa using SEM images. Using this length difference (SEM data (a-axis)) and the height of mesa (profilometer data (c-axis)), the angle between the basal plane and the side of the mesa can be calculated by Equation 4.1.

$$\theta(lateral \quad angle \quad of \quad mesa) = \tan^{-1}\left(\frac{profilometer \quad data \quad (c-axis)}{SEM \quad data \quad (a-axis)}\right) \tag{4.1}$$

The edges of mesa are labeled as can be seen in Figure 4.3 and the angles corresponding to these numbers are shown in the Table 4.1. For all fabricated mesas, the lateral angles are almost 50 degrees. It is not clear yet how the actual cross section of the mesa affects the resonant condition and emission power of the mesa. It is believed

that while right angles between the basal plane and the mesa sides should induce more intense power, the frequency tunability of the mesa may be not as large as for the trapezoidal cross section.

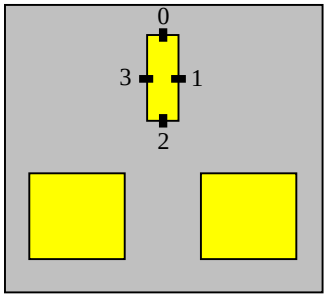

Figure 4.3. Labeled codes of mesa edges

Table 4.1. Height of mesas and deposited thin films

	Mesa dimension	**Au height 1**	**Co height**	**Au height 3**	**Mesa height (Only Bi2212)**		**Lateral angle**	
					1	**3**	**1**	**3**
FT06	100x300 μm^2	8 nm	60 nm	100 nm	333 nm	293 nm	-----	52.6°
FT08	100x300 μm^2	8 nm	60 nm	100 nm	301 nm	358 nm	-----	-----
FT13	55x300 μm^2	8 nm	60 nm	100 nm	563 nm	463 nm	-----	54.6°
FT34	55x300 μm^2	12 nm	60 nm	100 nm	802 nm	774 nm	48.6°	48.9°

Main reason of trapezoidal shape of mesas is thick photoresist layer because ions are accelerated through the mesa with angle of 67.5° and thick photoresist shades the region at the edge of the mesa against the ion beam etching. Thus while mesa height is increasing with increasing etching time, mesa starts to spread out and mesa with trapezoidal shape is obtained.

4.2. Electrical Results

4.2.1. Temperature Dependence of c-axis Resistance in Bi2212

c-axis resistance versus temperature (R-T) characteristics of the as-grown Bi2212 mesas were measured in a He flow cryostat system. This measurement gives very useful information to check the condition of the mesa such as the contact resistance, the sample quality and the doping level. R-T measurements of some of the fabricated mesas are seen in Figure 4.5, Figure 4.6, Figure 4.7 and Figure 4.8, that are belong to samples FT06, FT08, FT13 and FT34, respectively.

The sharp phase transitions from normal state to superconducting state are seen in all R-T graphs. The curves exhibit a typical temperature dependence of the c-axis resistance of Bi2212 single crystal. The onsets of critical temperatures of the mesas are between 91.5 and 95 K. Both temperature dependence of the resistance and the superconducting transition temperatures of the mesas indicate that FT06 and FT13 are in the near optimally doped state and FT08 and FT34 are in the near underdoped state of the Bi2212 crystals. The transition width, ΔT_c, is mostly 4–7.5 K. Transition temperatures and their transition width values of the samples are shown in Table 4.2.

Table 4.2. Electrical properties of the mesas

	$R_{Tc(onset)}$	$R_{300\ K}$	$R_{contact}$	$R_{Tc}/R_{300\ K}$	$T_{c(onset)}$	ΔT_c
FT06	7.88 Ω	6.99 Ω	0.85 Ω	1.13	93.5 K	4.00 K
FT08	25.3 Ω	13.9 Ω	4.50 Ω	1.82	93.0 K	43.1 K
FT13	8.86 Ω	6.66 Ω	2.00 Ω	1.33	95.0 K	4.00 K
FT34	60.7 Ω	30.7 Ω	9.50 Ω	1.97	91.5 K	7.50 K

As seen in all R-T graphs the mesa resistance is finite even below T_c. It is not a temperature dependent electrical behavior proper to superconducting crystal. This is because of the contact resistance due to three-point measurement configuration. This configuration is not generally preferred to four point contact method for accurate

measurement because there is one contact probe on mesa which is used for both applying current and measuring voltage and it causes reading surface resistance at superconducting state. However four point contacts is very difficult to fabricate on small area of mesa. For all fabricated samples, contact resistance is usually smaller than a few ohms. Therefore, it seems not to influence the measurement, but it may contribute to the heating.

The reason of contact resistance is the interface between gold layer and surface of Bi2212 as shown in Figure 4.4. This kind of contact resistance increases at low temperatures, because the interface behaves like tunneling barrier. Assuming that the contact resistance is weakly dependent on temperature above T_c, the $R(T_c)/R(300\ K)$ values in Table 4.2 give at least a hint. For all fabricated mesas, the ratios of $R(T_c)/R(300\ K)$ are between 1.1 and 2. All THz emitting mesas are below a certain underdoped level of Bi2212 and their $R(T_c)/R(300\ K) > 4$ that indicates a necessity of a certain doping range of $\delta \cong 0.22$ for THz emission (Ozyuzer, et al. 2009). Therefore, fabricated mesas have high doping level for THz emission.

Figure 4.4. Side view of mesa to show the contact surface resistance between gold layer and surface of Bi2212

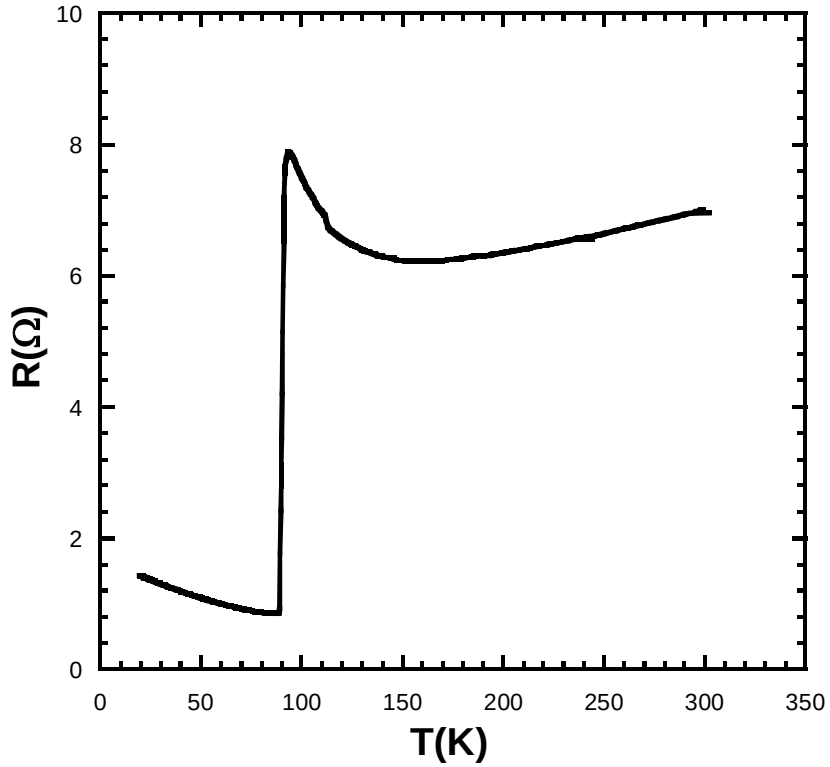

Figure 4.5. Resistance versus temperature behavior of FT06

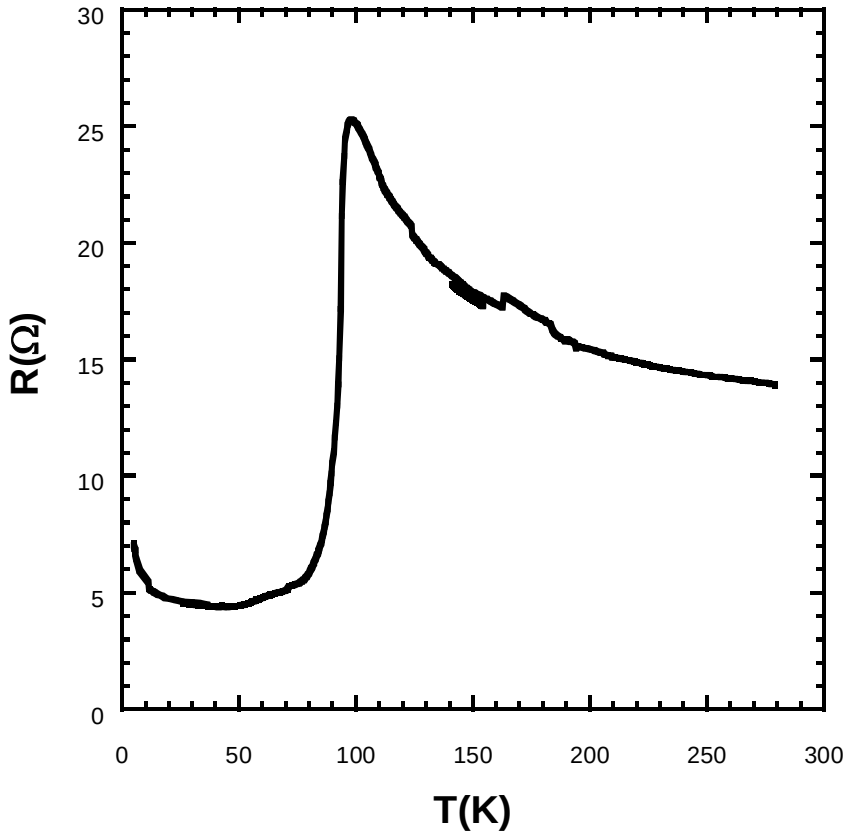

Figure 4.6. Resistance versus temperature behavior of FT08

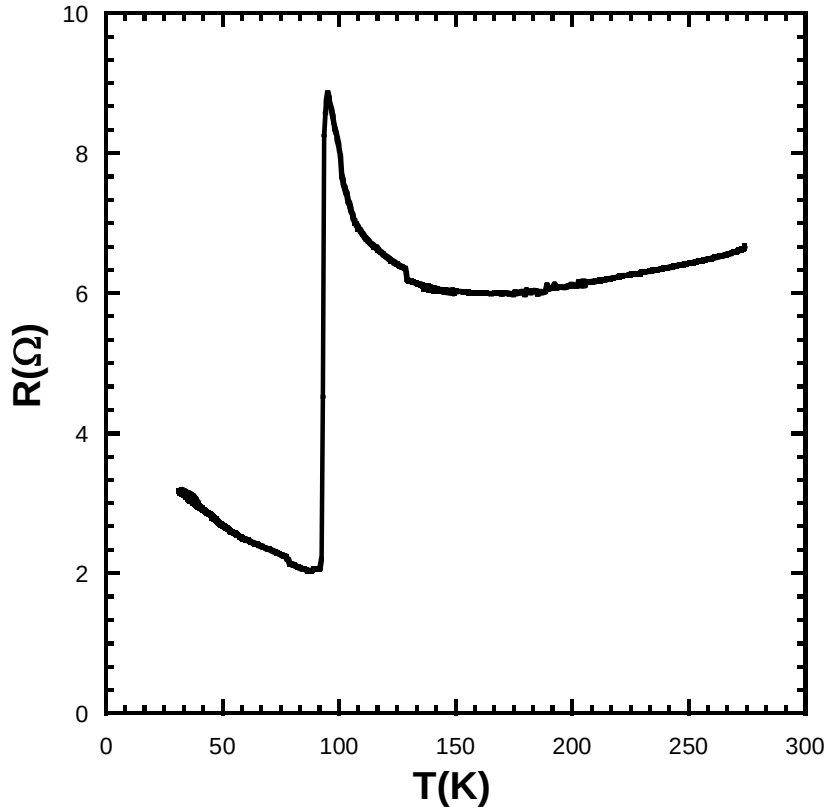

Figure 4.7. Resistance versus temperature behavior of FT13

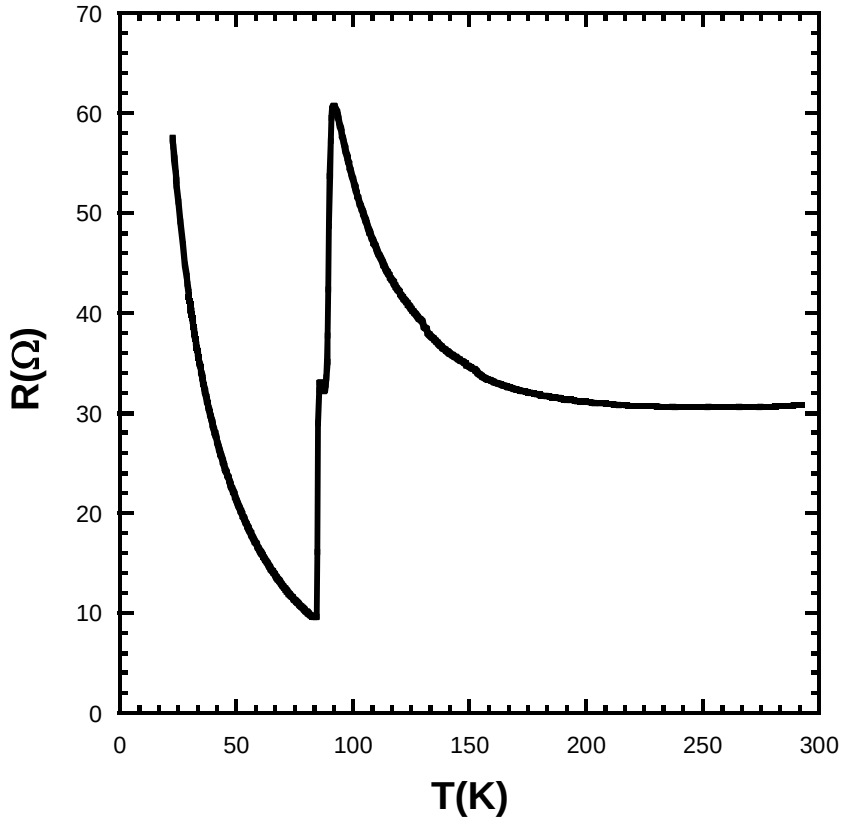

Figure 4.8. Resistance versus temperature behavior of FT34

4.2.2. Tunneling Characteristic of Bi2212 Single Crystal

Figure 4.9 and Figure 4.10 show current voltage characteristics of FT13 and FT34, respectively. Both measurements were taken at 4.2 K. I-V characteristic of Bi2212 mesas show a number of characteristic features of the multi stacked intrinsic Josephson junction. They include several branches due to individual switching of each junction from Josephson state to quasiparticle state when the bias current exceeds the individual critical current of each junction (Yurgens 2000). Thus each of the junctions acts as one of the single branch. To obtain different quasiparticle branches, the bias voltage is continuously swept positively and negatively many times. While bias voltage increases, these branches appear such a voltage jumps until all IJJs are completely in normal state. While decreasing bias voltage, I-V data does not trace these branches because there is a transition from normal state to superconducting state. This leads to hysteresis in the I-V characteristics.

In order to obtain as much as more quasiparticle branches in I-V, the swept frequency should be low while ac bias current on mesa is swept negatively and positively by function generator. In our measurement, it was between 0.1 and 5 mHz to catch more branch and has triangle wave form. Also the output amplitude of function generator was gradually increased in order not to allow the heating in mesa due to high bias current.

Normally, if all IJJs are more identical with respect to critical current and junction area, distances between branches should have a same gradual current rise and the voltage jump, therefore, superconducting energy gap of an individual SIS junction can be found by dividing sum-gap voltage to the number of IJJs. However, our fabricated mesas have too many IJJs. Such more IJJs cause more heating in mesa and more heating makes equidistance of voltage jumps become disarray (Yurgens 2000). If Figure 4.9 and 4.10 are examined, it can be seen that these spaces between quasiparticle branches become smaller as being approached to higher bias values. Therefore, calculation of the energy gap from I-V graph becomes difficult.

Both of I-V curves of FT13 and FT34 show backbending at high bias voltages, (957 mV for FT13 and 1580 mV for FT34), where heating severely affects the local mesa temperature. The backbending of the I-V curve at high currents is due to self-heating effects as indicated by the appearance of unpolarized blackbody radiation. The

back-bending voltage of large area mesas depends on doping level of Bi2212, number of junctions and surface area of the mesa (Zhu, et al. 2006). It has been shown that in IJJ stacks the heating can be precluded by lowering the number of junctions and by decreasing the mesa area. Unfortunately, these also decrease the power and conflict with the resonance condition in our case.

It is observed that all THz emitting mesas are below a certain underdoped level, which has relatively small critical current density (~100 A/cm^2) in contrast to optimally doped and overdoped Bi2212 (Ozyuzer, et al. 2009). The necessity of small critical current density is due to decrease the influence of heating effect on emission.

Detailed graphs of both FT13 and FT34 reveal Josephson current exactly (Figures 4.9.b and Figure 4.10.b). The magnitude of Josephson critical current is 60 mA for FT13 and 18 mA for FT34 when spin polarized current is injected through the c-axes of the as-grown mesas. Josephson critical current density, J_c, is 364 A/cm^2 for FT13 and 120 A/cm^2 for FT34. We observed decrease in J_c, which is between 1000 and 2000 A/cm^2 for as-grown Bi2212 crystals, due to injection of spin polarized current. It was also demonstrated by previous thesis in our group by comparing spin degenerate and spin polarized cases (Ozdemir 2006). We can obtain small J_c as low as THz emitting mesas from as-grown mesas using spin polarized current. However, we cannot limit decrease in critical current.

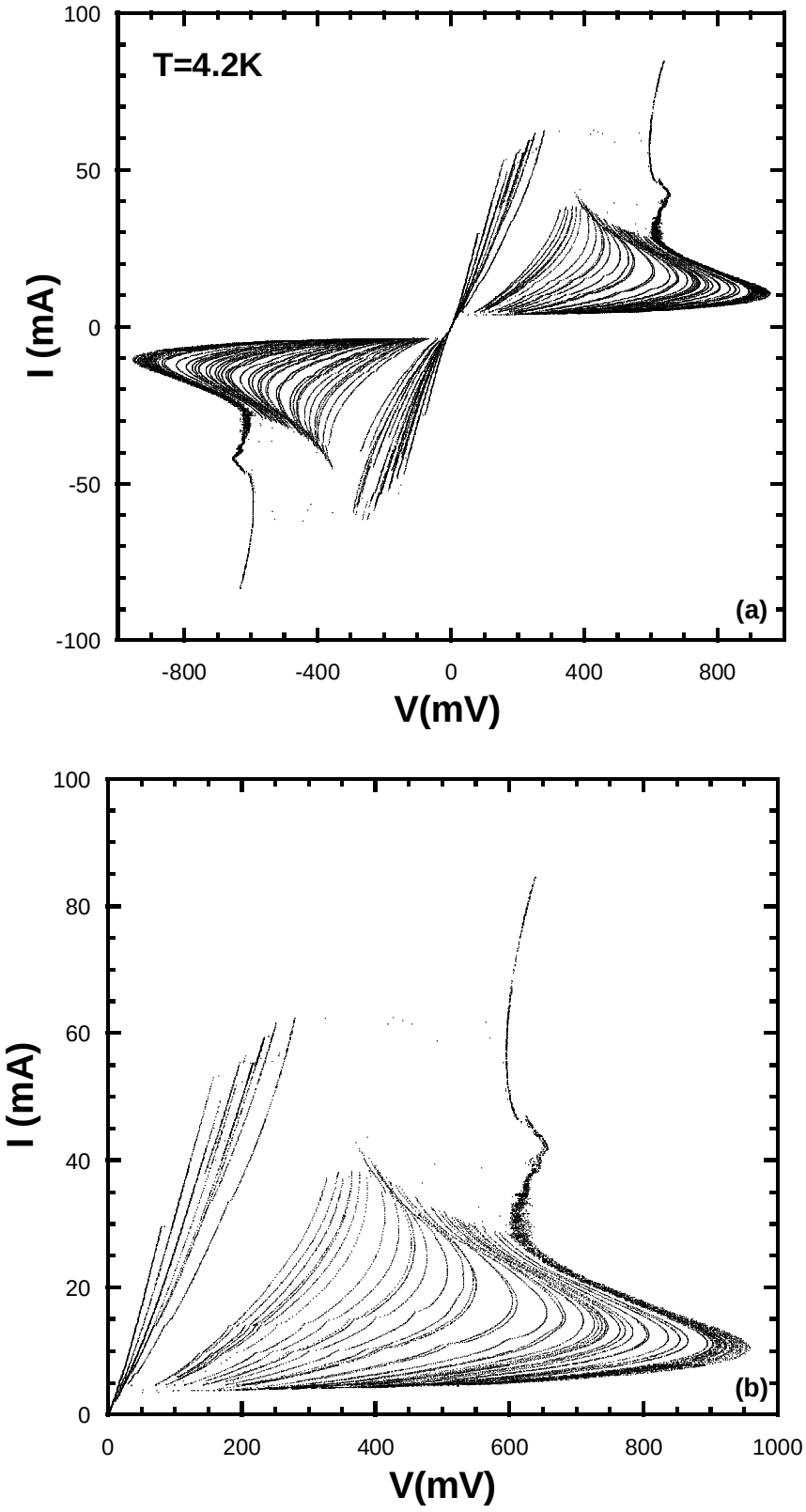

Figure 4.9. I-V measurement of FT13 (a) and its detailed graph (b)

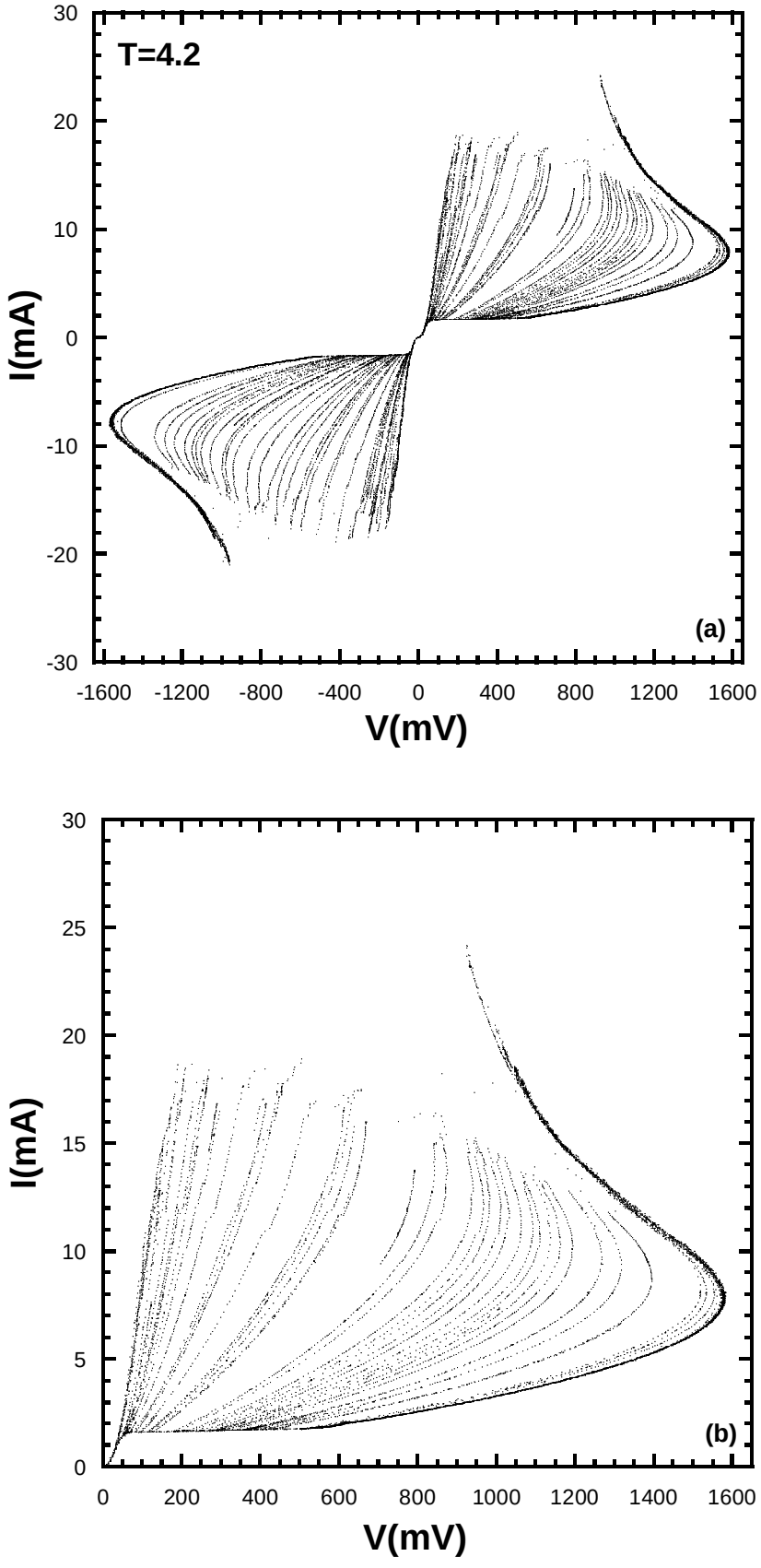

Figure 4.10. I-V measurement of FT34 (a) and its detail graph (b)

4.3. Bolometric Detection of Radiation from Mesa

A significant radiation at THz frequency range can be obtained out of long edge of mesa on Bi2212 single crystal in zero magnetic field (Ozyuzer, et al. 2007). It results from oscillating current due to voltage drop across the IJJs and it is based on ac Josephson effect. Since it is expected that the radiation is emitted from long edge of tall mesa, emission was detected by Si bolometer from long edge of mesa, while ac current with low swept frequency is applying along the c-axis of Bi2212 single crystal. Since the radiation emitted from Bi2212 results from recombination of pairs supremely, ac current with less swept frequency were applied during decreasing bias voltage. Against the influence of variation at ambient temperature on bolometer response, the system was thermally isolated to reduce the background of spurious count. Background was subtracted by lock-in for sensitive detection. However, our bolometer is sensitive to thermal radiation, so, joule heating occurs because of non-equilibrium quasiparticle tunneling in large and tall mesas at high bias voltages.

THz emission characteristics were obtained during I–V scans and recorded simultaneously. This gives us information on how the I–V looks like before and after THz emission. Figure 4.11 and Figure 4.12 shows THz emission characteristics and current voltage characteristics of FT13 and FT34, respectively. Both measurements were taken at 22 K. When I-V curves of FT13 and FT34 show backbending, the bolometer detects the heating of the mesa in the form of unpolarized black body radiation. As can be seen in Figure 4.11, there are no emission peak detected by bolometer for FT13. The c-axis quasiparticle conductivity, and therefore dissipation and self-heating, is too high for this sample. Therefore, the major problem of non-emission can be heating problem which cause desynchronization of Josephson oscillations in junctions. THz radiation can be obtained before heating severely affects the local mesa temperature. The width of 55 μm corresponds to an emission frequency of roughly 0.779 THz for this sample, which, according to the Josephson voltage-frequency relation, occurs at 551 mV for 342 junctions. This value is inside the heating region as seen in Figure 4.11, where the heating causes local temperature increases seen the in I-V curve of mesa.

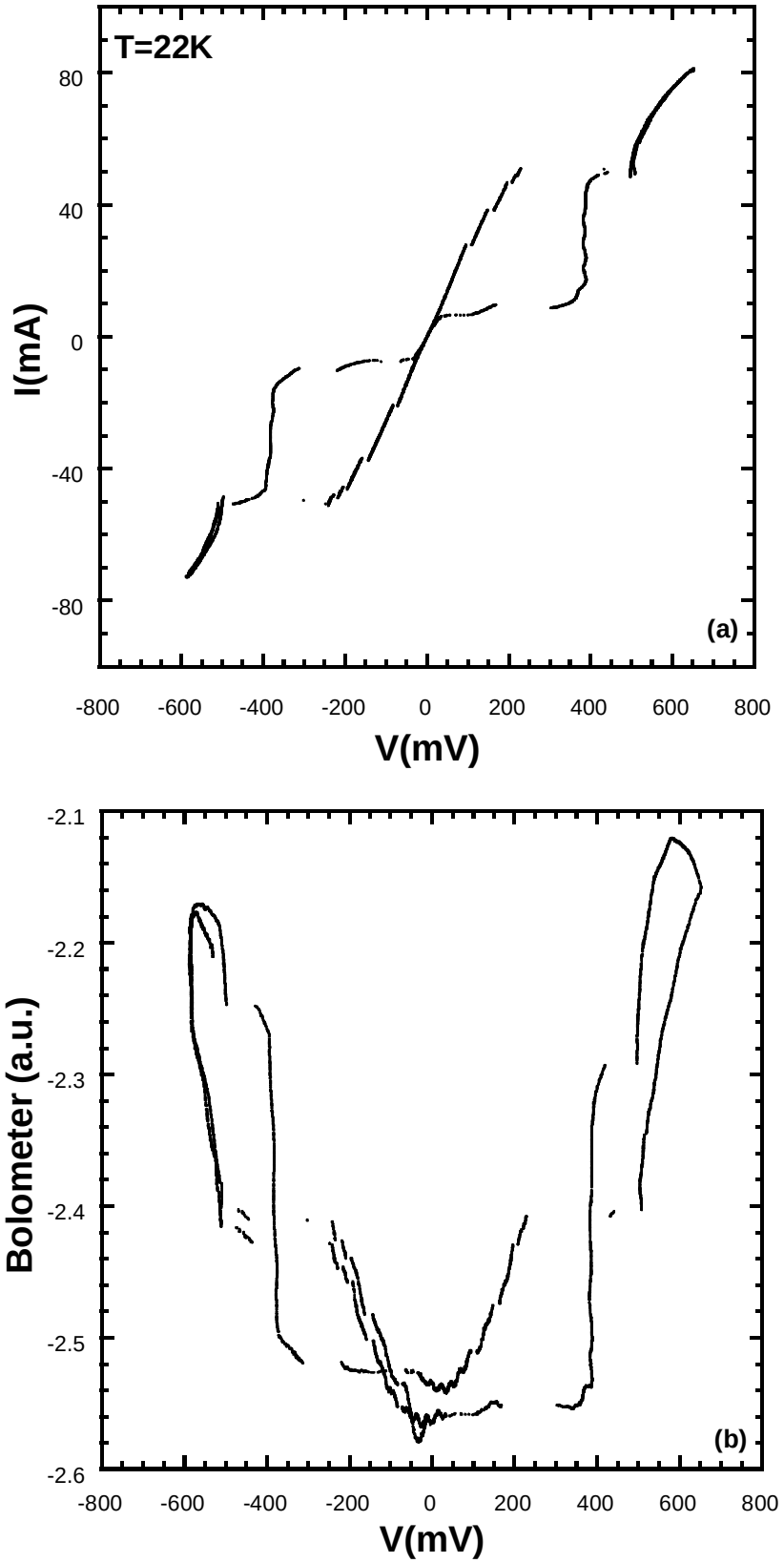

Figure 4.11. I-V (a) and Bolometer (b) measurements of FT13 at 22 K

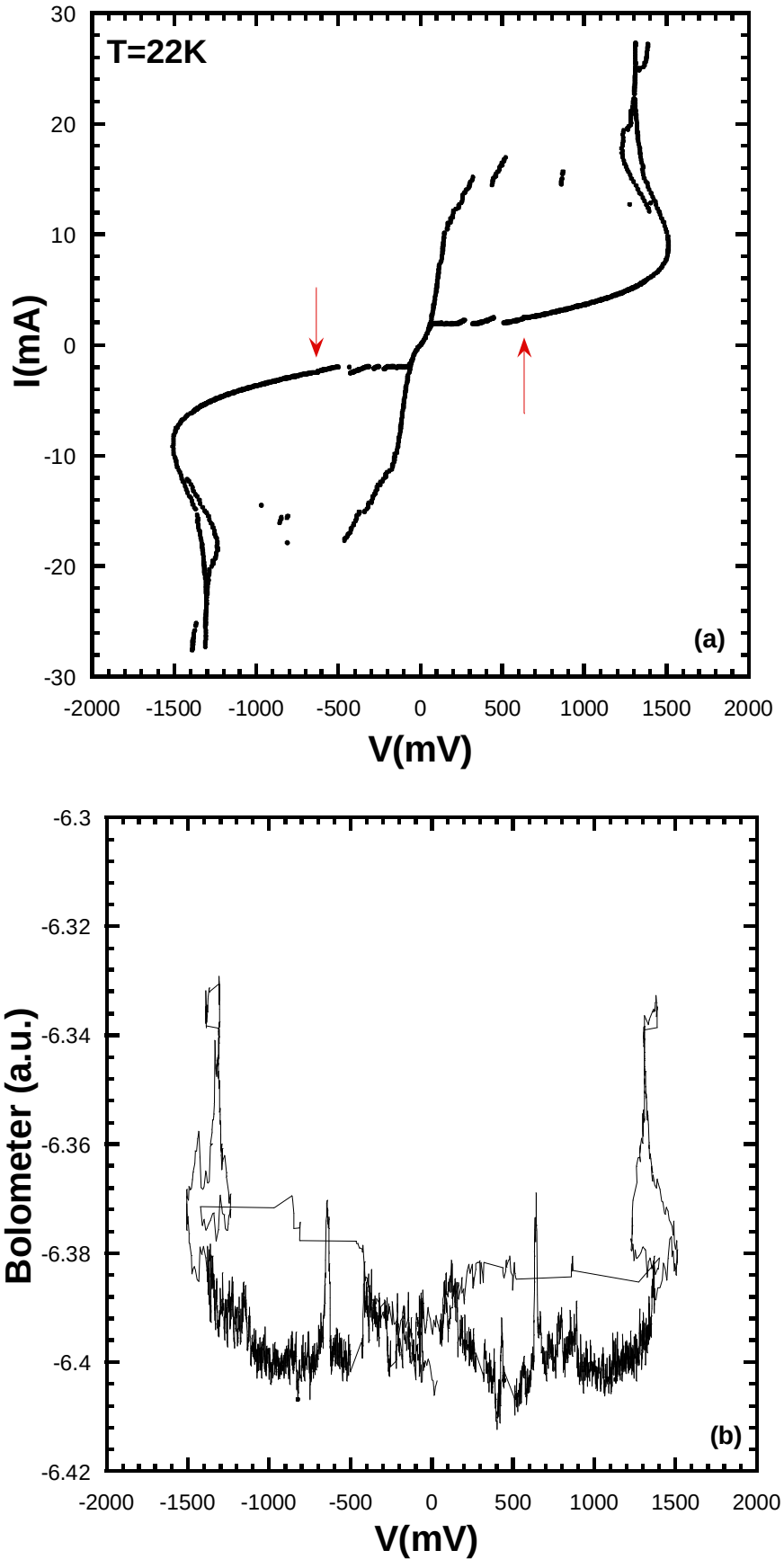

Figure 4.12. I-V (a) and Bolometer (b) measurements of FT34 at 22 K

We observed THz emission peak for FT34 which has low quasiparticle conductivity and low dissipation due to its small critical current density. It means that the adjustment of doping level can be eliminated for successful THz emission by the injection of spin polarized current through the c-axes of the as-grown mesas. Figure 4.12.b displays emission peaks for positive and negative bias voltages. When all junctions, roughly 534, are in the resistive state and the bias is decreasing slowly, the bolometer begins to give a response at 0.66 V. Further decreasing the bias, the signal reaches a peak position around 0.64 V. On the bias decreasing part of the I-V curve at low bias there are some jumps, which occur as some junctions switch to the zero voltage state (Figure 4.12.a). These jumps are called as re-trapping. We did not observe re-trapping event in the emission region, this indicates that there is no loss of emission.

When we look at the emission region (arrows in Figure 4.12.a), we see the bump in return branch due to radiation (Figure 4.13). That is emission persist over an extended voltage range around the resonance condition. This property is a consequence of non-rectangular cross-section of the resonators and allows for the design of THz sources with voltage-tunable emission frequencies (Gray, et al. 2009).

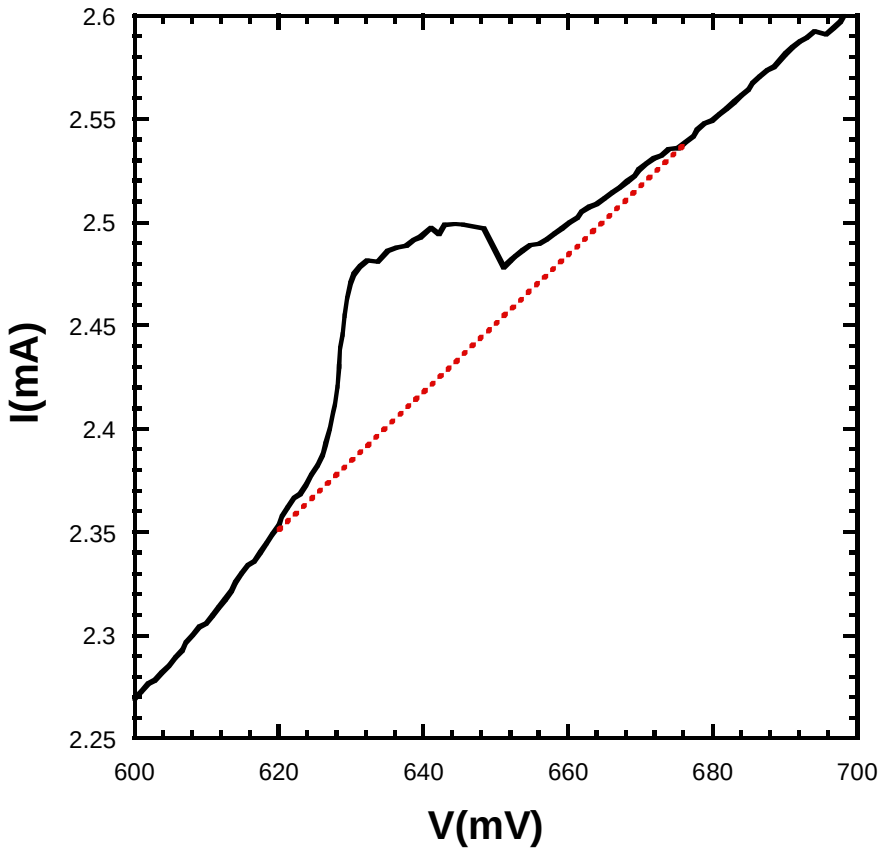

Figure 4.13. Close-up of the return branch of I-V curve

4.4. Emission analyses

4.4.1. Emission Frequency

THz interferometer setup was used to find the emission frequency of FT34. Figure 4.14 shows the interferometer setup. When we apply certain voltage in the emission region, this set up splits a single wave coming from long edge of mesa, then brings the constituent waves back together so that they superpose, forming an interference pattern.

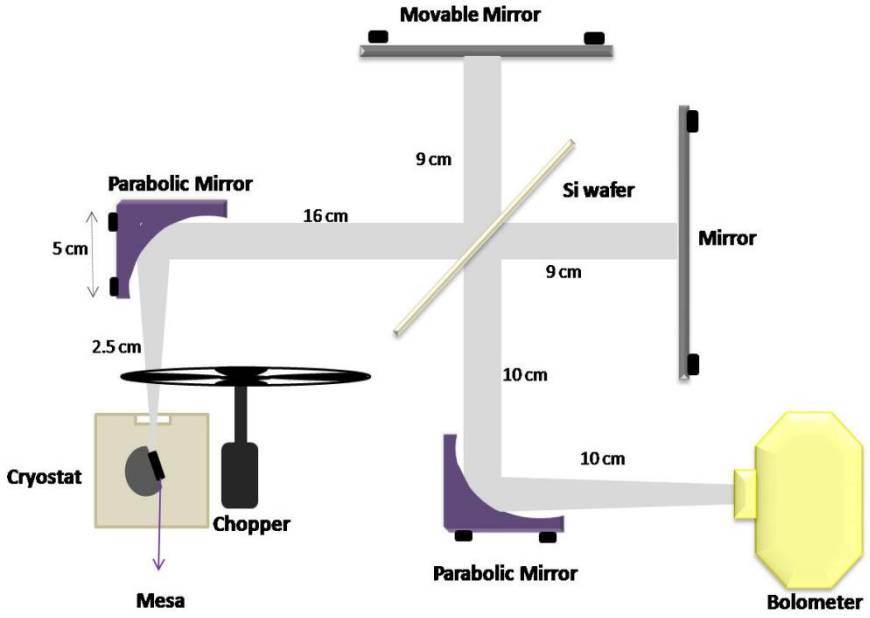

Figure 4.14. THz interferometer setup

Waves travel from the mesa to the Bolometer over two different paths. In one path, the wave reflecting from parabolic mirror passes directly through Si wafer, reflects back to Si wafer from fixed mirror, and then is reflected from Si wafer into the Bolometer. In the other path, the wave reflecting from parabolic mirror reflects from Si wafer into movable mirror, and then back through Si wafer into the Bolometer. If the two waves are in phase when they reach the Bolometer, a maximum signal is detected. By moving movable mirror, the path length of one wave changes, thereby changing its phase at the Bolometer so a maximum is no longer detected. Since each wave passes twice between mirrors and the Si wafer, moving movable mirror a distance $\lambda/2$ will

cause a complete 360° change in the phase of one wave at the Bolometer. This cause passes through a minimum and return to a maximum. Figure 4.15 shows the signals detected by bolometer.

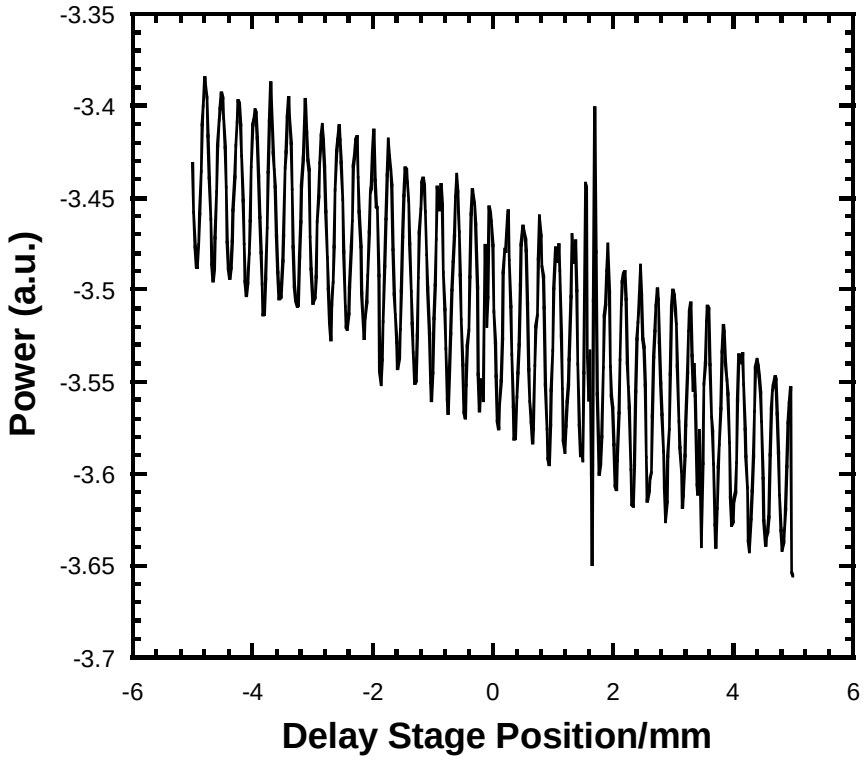

Figure 4.15. Interference patterns detected by bolometer inside the emission region

When we take the fast Fourier transform (FFT) of this wave form using Labview program, we can find the emission frequency. Figure 4.16 shows the result of the frequency spectrum of the emission and the peak in this figure indicates that emission frequency of FT34 is 0.537 THz. Here, the full width at half maximum (FWHM) of the peak is 31.3 GHz. This quite large value is attributed to the instrumental origin because instrumental resolution is not good enough. Moreover, there are some technical difficulties, for example, we cannot keep the voltage constant during the measurement.

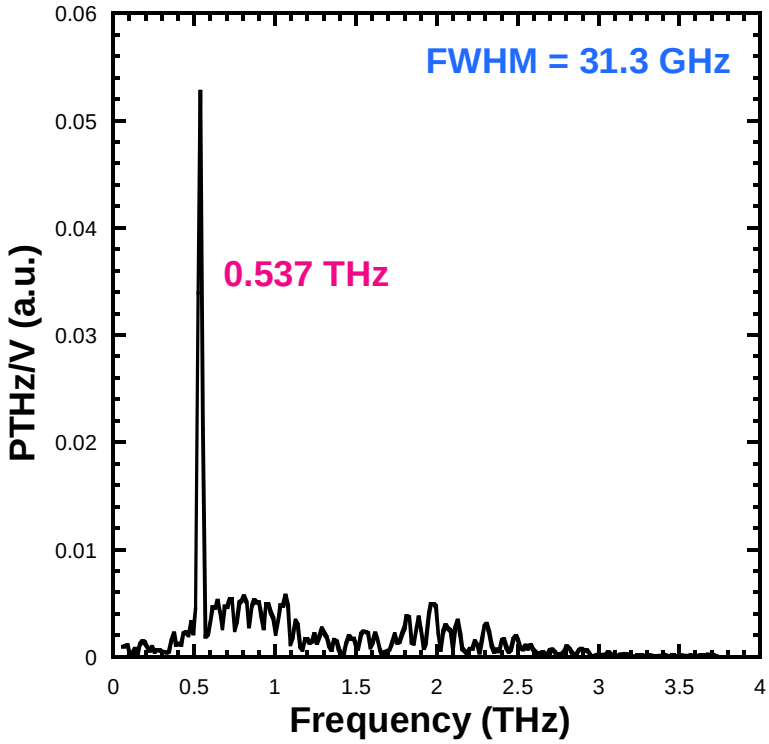

Figure 4.16. The frequency spectrum of the emission observed from the w = 55 μm mesa

In Figure 4.17, interference patterns cannot be observed after a certain point because applied voltage is outside the emission region.

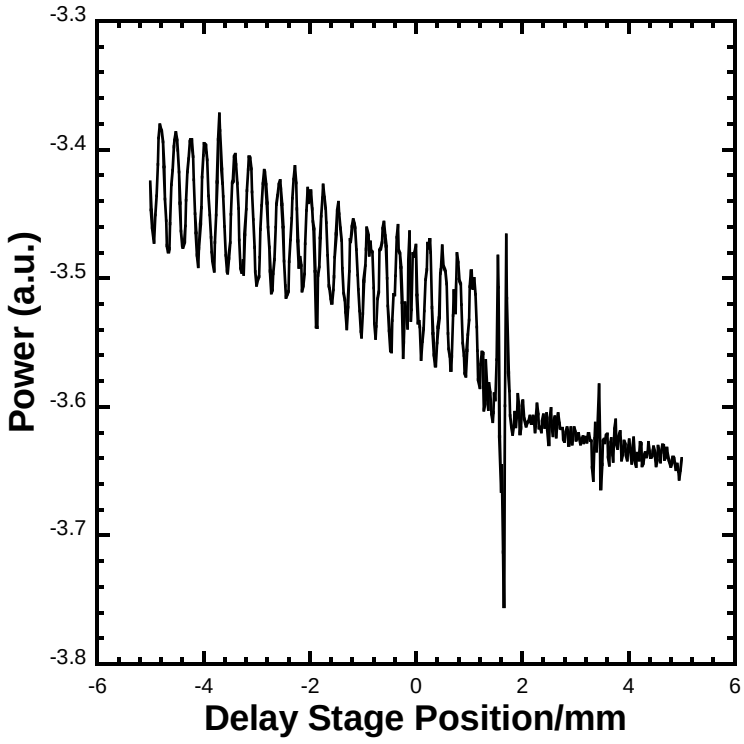

Figure 4.17. Signals detected by bolometer inside and outside the emission region

4.4.2. Aging of Contact Resistance

In order to ensure the emission from superconducting mesa structure, bolometric output peaks should be reproducible for each scanning of bias voltage decreasing toward to zero. Therefore I-V measurements were allowed to be repeated severally. Figure 4.18 show four different I-V scans of FT34 obtained in couple of week periods. We observed that contact resistance increases in each scan; it may be due to degradation of single crystal surface by thin Au layer.

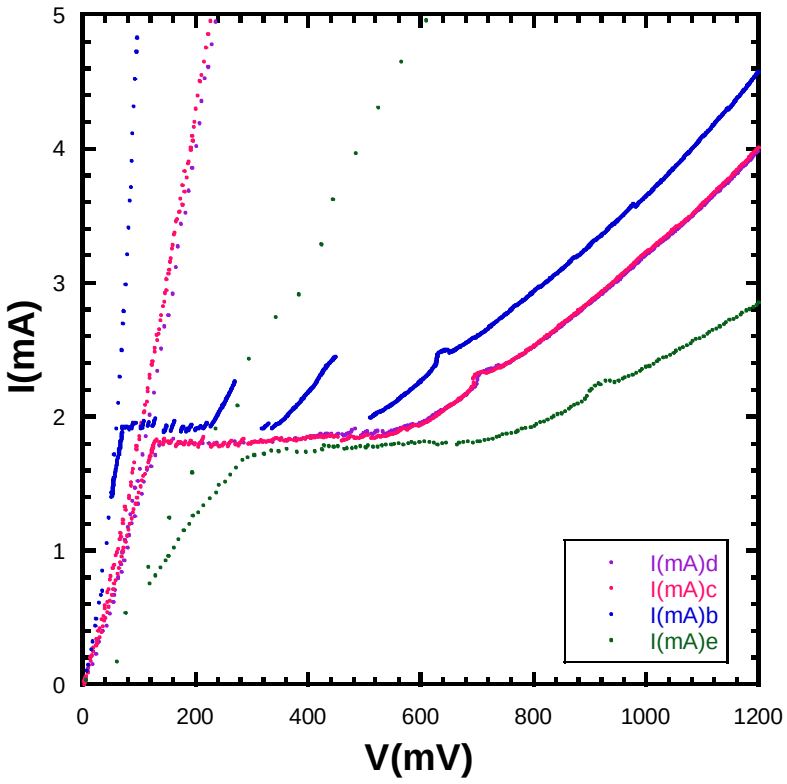

Figure 4.18. Different I-V scans of FT34

If we subtract the contact resistances from I-V curves (Figure 4.18), the voltages of the bumps decrease to nearly 586 mV (Figure 4.19). It has shown previously that the fundamental frequency satisfies the ac-Josephson relation, $f = V_{jct} / \Phi_0$, where Φ_0 is the flux quantum and V_{jct} is the voltage per junction (Ozyuzer, et al. 2007). According to the Josephson voltage-frequency relation, emission frequency is roughly 0.530 THz which occurs at 586 mV for 534 junctions. This is nearly equal to THz interferometer result, so it satisfies Josephson voltage-frequency relation.

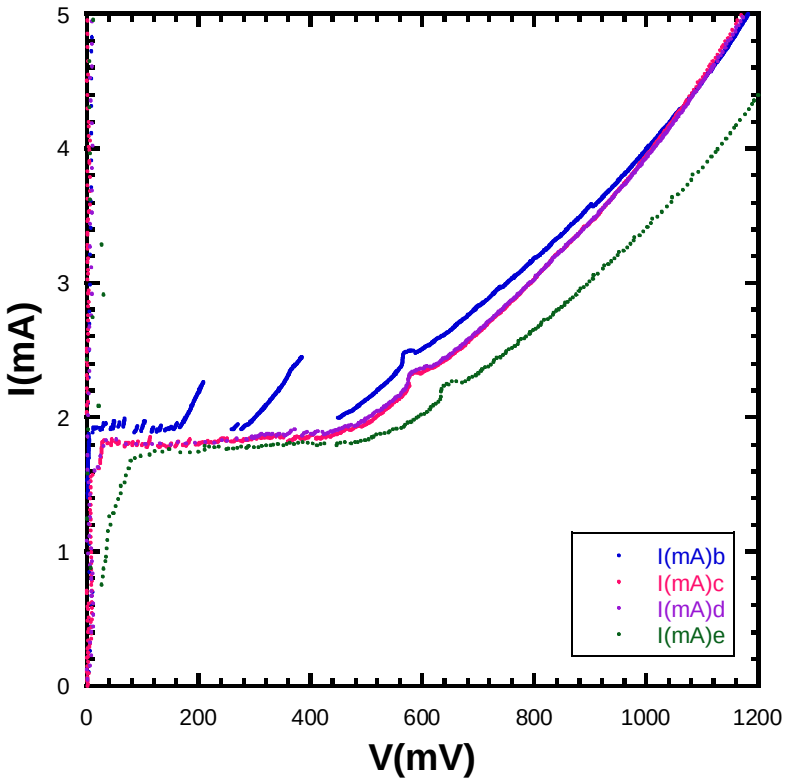

Figure 4.19. Different I-V scans of FT34 without contact resistances

Since the width of mesa (w) is comparable to the wavelength of the plasma waves, mesa renders itself as a cavity. By varying the applied dc voltage V across the mesa, the frequency of the THz radiation appears to be locked by a cavity resonance, which fixes it to that of one of the standing wave modes inside the mesa. In most of the experiments on rectangular samples, radiation has been found to occur when the Josephson frequency of the IJJ matches frequency of fundamental cavity resonance mode, $f=c_0/2nw$, where w is the width of the mesa, n is the c-axis far-infrared refractive index of Bi2212, and c_0 is the speed of light in vacuum. Refractive index of Bi2212 was obtained as 4.2 from the slope of the fundamental frequency versus 1/w plot of different THz emitting mesas (Kadowaki, et al. 2010) and obtained as 3.5 by infrared spectroscopy (Gaifullin, et al. 2000). 0.537 THz emission frequency corresponds to n=5.1 according to frequency of fundamental cavity resonance mode. This quite large value may be attributed to the doping level and composition of the crystal. The width of 55 µm corresponds to frequency of roughly 0.779 THz for n=3.5 and 0.649 THz for n=4.2. The emission frequency of FT34 is not in good agreement with the frequency of fundamental cavity resonance for n=3.5 and n=4.2, so, it may be higher cavity resonance mode.

4.4.3. Estimation of Emission Power

Maximum bolometer response value of the emission peak can be seen also in the unpolarized thermal radiation region at 1410 mV as shown in Figure 4.20. If we think this thermal radiation detected by the bolometer as blackbody radiation from the mesa, we can estimate the emission power. To do so, we need to determine the local temperature of unpolarized infrared radiation at 1410 mV. Therefore, firstly we found the value of the resistance at 1410 mV, which equals V/I, along the I-V curve (Figure 4.21). However, such a high resistance cannot be observed in temperature-dependent mesa resistance of Figure 4.8, so, we extrapolated it to lower T as shown in Figure 4.22 and we determined the temperature of unpolarized radiation as T= 71.9 K.

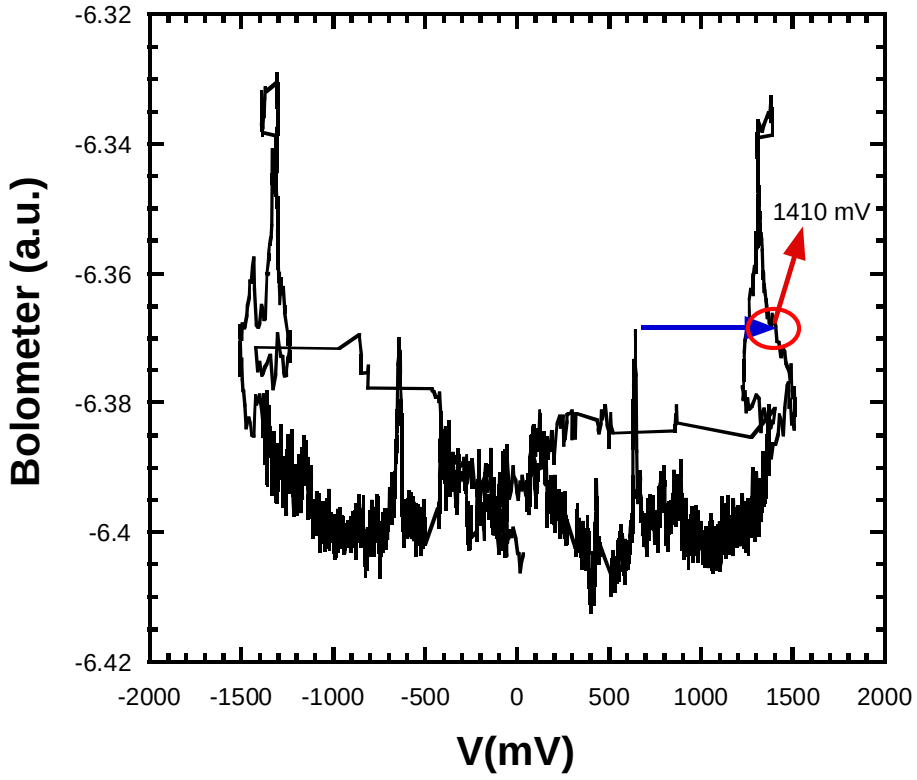

Figure 4.20. Maximum bolometer response value of the emission peak in the unpolarized thermal radiation region

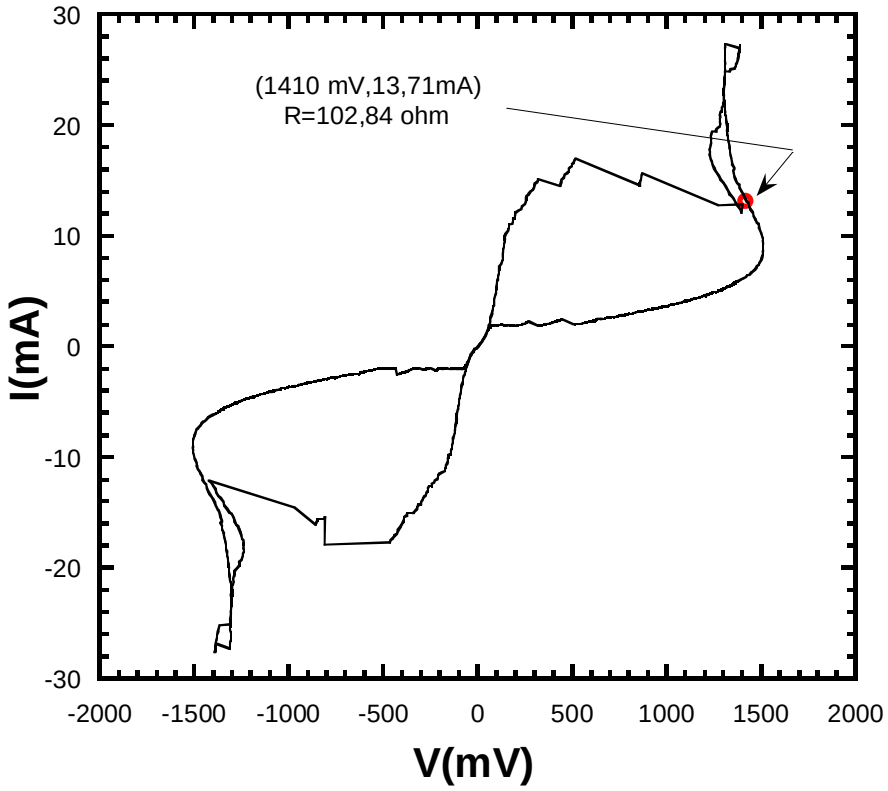

Figure 4.21. Determination of resistance in the unpolarized thermal radiation region from I-V curve

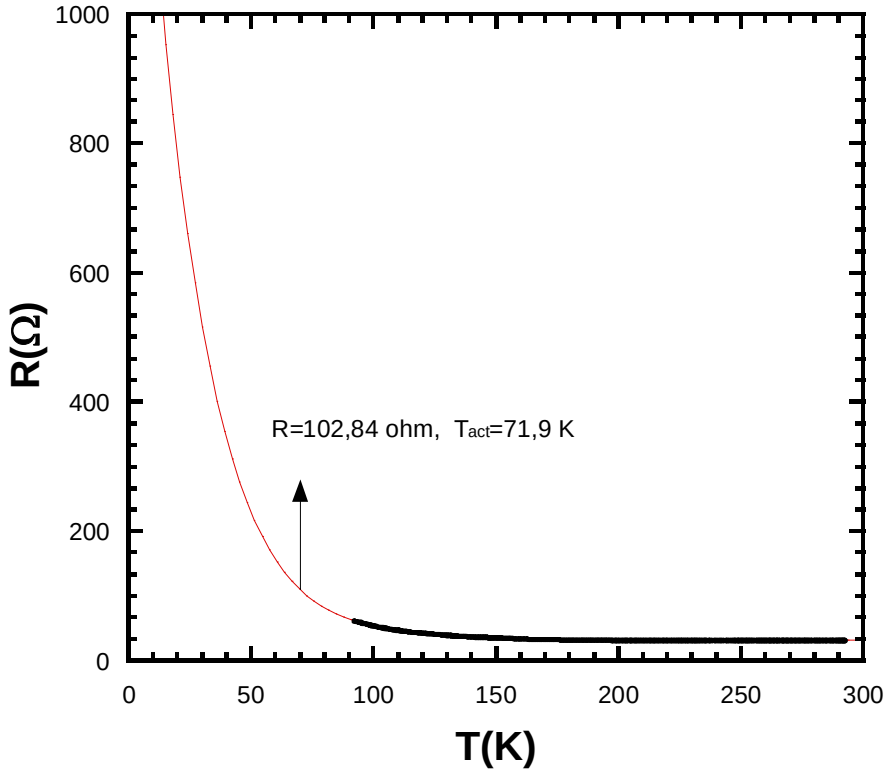

Figure 4.22. The extrapolation of resistance versus temperature behavior of FT34 to lower temperature

This temperature was used to calculate expected blackbody radiation from the Bi2212 surfaces. The emitted power is given by the modified Stefan-Boltzmann law

$$P_B = eA\left(\frac{\Omega}{2\pi}\right)\sigma F(T)T^4 \tag{4.2}$$

where e is the emissivity (assumed equal to 1), A is the area of the entire crystal (not just the mesa) facing the detector and $\sigma = 5.67\ 10^{-8}$ J/secm^2 K^4 is the Stefan-Boltzmann constant. The function F(T) accounts for the fact that a low-pass filter suppresses radiation to the bolometer for wavelengths less than 120 microns. With this filter, the response function, $F(T)T^4$, is 0.8 T^4 at low temperatures and approximates $6.4x10^4$ K^3 (T-27.5 K) for the range from 40 to 150 K (Kurter, et al. 2009). So we used $F(T)T^4=6.4x10^4$ K^3 (T-27.5 K) for T=71.9K . Assuming we collect all the radiation (solid angle $\Omega\cong 2\pi$), we get 72.6 nW peak power.

In order to estimate the total power emitted from the sample, the geometrical configuration of the equipments should be taken into account. A schematic of the optical set-up is shown in Figure 4.23. The emitted radiation is guided by Copper tubes which have π cm^2 cross section area, that is, bolometer detects only some part of the radiation. If we assume mesa as a point source, emission area should be equal to $4\pi r^2=64\pi$ cm^2. This, therefore, leads to a value of P= 4.65 µW.

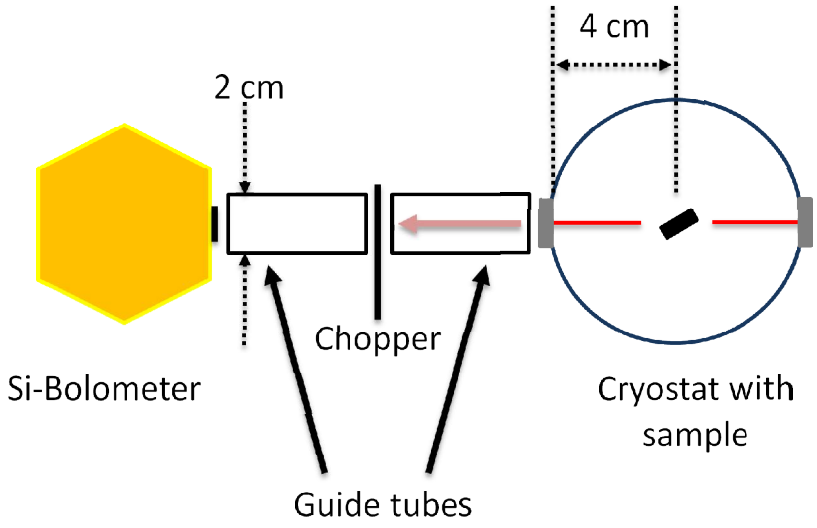

Figure 4.23. Schematic of the optical set-up

Figure 4.24 shows a close-up of the return branch of I-V curve. The absence of a jump in the I-V curve allows us to establish a baseline of the current and to determine the excess current that supplies the energy for the excitation of the cavity resonance. These data suggest that about 57 μW are pumped into the in-phase resonance. Since the estimated total power is 4.65 μW, only 8.1 % of the total dc power dissipated in the mesa. This implies that considerably enhanced radiation powers could be obtained with this mesa, for example, through improved impedance matching with the help of antennas, gratings, or dielectric coatings. Moreover, to be more precise, we should take into account angular dependence of the emission power (Kadowaki, et al. 2009).

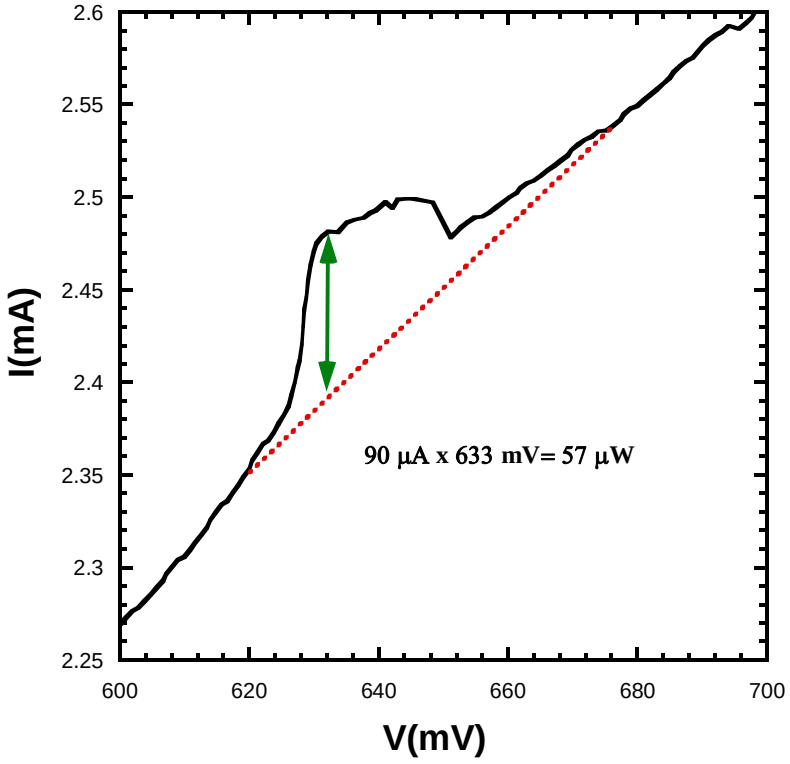

Figure 4.24. Determination of the power pumped into the in-phase resonance by the excess current from I-V curve

CHAPTER 5

CONCLUSION

In this work, rectangular Au/Co/Au/Bi2212 mesas with large areas and high thicknesses were fabricated on as-grown Bi2212 single crystals by various experimental processes. The lateral angles and heights of mesas were analyzed by SEM and profilometer. After that, c-axis resistance versus temperature and current-voltage tunneling characteristics were investigated in a He flow cryostat system. Finally, emission characteristics were obtained and emission analyses were done.

In long mesa fabrication processes, firstly, single crystal of Bi2212 is glued onto a sapphire substrate by silver epoxy. In order to get a fresh and smooth surface on Bi2212, the crystal was then cleaved with an adhesive tape and Au layer with the thickness of 8 nm was thermally deposited on the cleaved crystal surface immediately to prevent the chemical reactions between Co layer and Bi2212 crystal. Increasing thickness of the Au layer causes the reduction of spin polarization of the quasiparticles so thin Au layer was used to keep polarization of spins. After that 60 nm Co layer was deposited on thin Au layer as a spin injector and then in order to prevent oxidation 100 nm thick Au layer was deposited on the top of Co layer. 55x300 μm^2 and 100x300 μm^2 mesa structures, their heights were up to 800 nm, were fabricated on crystals using standard optical photolithography and Ar ion beam etching techniques. Because of the difficulties in making a contact on small area of the mesa, firstly CaF_2 insulating layer is deposited by evaporation onto crystal and small area of the mesa then a gold stripe with the width of 30 µm was created by lift-off technique on the mesa and CaF_2 layer. Finally three gold probe wires are connected to the two contact paths and mesa by silver epoxy. The contact on mesa was used as both the current and voltage leads.

In order to characterize the Bi2212 mesas, c-axis resistance versus temperature (R-T) and current-voltage (I-V) tunneling characteristics were investigated in a He flow cryostat system. R-T curves of fabricated mesas exhibit a typical temperature dependence of the c-axis resistance of Bi2212 single crystal. The onsets of critical temperatures of the mesas are between 91.5 and 95 K. Both temperature dependence of the resistance and the superconducting transition temperatures of the mesas indicate that

some of the mesas are in the near optimally doped state and the others are in the near underdoped state of the Bi2212 crystals. In all R-T graphs, we observed contact resistance due to three-point measurement configuration. Some of the hysteretic quasiparticle branches are observed in the I–V characteristics of as-grown Bi2212 crystals. At high bias where heating severely affects the local mesa temperature, back bending of the I-V curves were observed due to self heating of the mesas. We observed decrease in Josephson critical currents of mesas when spin polarized current is injected through the c-axes of the mesas.

Emission characteristics were obtained during I–V scans and recorded simultaneously. This gives us information on how the I–V looks like before and after emission. At high bias, I–V curves show backbending and the bolometer detects the heating of the mesas in the form of unpolarized black body radiation. When all junctions are in the resistive state and the bias is decreasing slowly, we observed emission peak near 0.61 V for one of the mesa which has low quasiparticle conductivity and low dissipation due to its small critical current density. It means that the adjustment of doping level can be eliminated for successful THz emission by the injection of spin polarized current through the c-axes of the as-grown mesas. However, we cannot limit decrease in critical current; so, we could not observe emission for the other mesa which has higher quasiparticle conductivity.

When we look at the emission region in the I-V curve, we see the bump in return branch due to radiation. That is emission persist over an extended voltage range around the resonance condition. This property is a consequence of trapezoidal cross-section of the mesa and allows for the design of THz sources with voltage-tunable emission frequencies.

THz interferometer setup was used to find the emission frequency of the mesa. When we apply certain voltage in the emission region, this set up splits a single wave coming from long edge of mesa, then brings the constituent waves back together so that they superpose, forming an interference pattern. Fast Fourier transform (FFT) of the interference patterns detected by bolometer indicates that emission frequency is 0.537 THz.

I-V scans were repeated severally to ensure the emission from superconducting mesa structure. We observed that contact resistance increases in each scan due to degradation of single crystal surface by thin Au layer. The contact resistances were subtracted from I-V curves and the voltage of the bumps decreased to nearly 586 mV.

According to the Josephson voltage-frequency relation, emission frequency is roughly 0.530 THz which occurs at 0.586 V for 534 junctions. This is nearly equals to THz interferometer result, so, it satisfies Josephson voltage-frequency relation. In contrast to previous works, we found higher refractive index (n= 5.1) according to frequency of fundamental cavity resonance mode for 0.537 THz emission frequency. For the refractive indexes obtained in previous works, the emission frequency is not in good agreement with the frequency of fundamental cavity resonance.

We calculated expected blackbody radiation from the Bi2212 surfaces by the modified Stefan-Boltzmann law. Assuming we collect all the radiation, we get 72.6 nW peak power. This leads to a value of 4.65 μW total power from the geometrical configuration of the equipments. We determined the excess current that supplies the energy and observed that about 57 μW power is pumped into the in-phase resonance and only 8.1 % of the total dc power dissipated in the mesa. This implies that considerably enhanced radiation powers could be obtained with this mesa, for example, through improved impedance matching with the help of antennas, gratings, or dielectric coatings.

REFERENCES

Abrikosov, A. A. 1957. On the Magnetic Properties of Superconductors of the Second Group. *Soviet Physics JETP* 5:1174

Akimitsu, J., A. Yamazaki, H. Sawa and H. Fujiki. 1987. Superconductivity in the Bi-Sr-Cu-O system. *Japanese Journal of Applied Physics* 26:2080.

Ambegaokar, V. and A. Baratoff. 1963. Tunneling between superconductors. *Physical Review Letters* 11:104.

Ambegaokar, V. and A. Baratoff. 1963. High temperature superconductors: Processing and science. *Physical Review Letters* 10:486.

Anderson, J. R. and J. M. Rowell. 1963. Probable observation of the Josephson superconducting tunnel effect. *Physical Review Letters* 10:230

Arnone, D. D., C. M. Ciesla, A. Coricha, S. Egusa, M. Pepper, J. M. Chamberlain,C. Bezant, R. Clothier and N. Khammo. 1999. Applications of terahertz (THz) tech-nology to medical imaging. Terahertz Spectroscopy and Applications II, ed. by J. M.Chamberlain. *Proceedings of SPIE* 3828:209–219

Aronov, A. G. 1976a. Spin injection and polarization of excitations and nuclei in superconductors. *Zh. Eksp. Teor. Fiz.* 71:370–376

Aronov, A. G. 1976b. Spin injection in metals and polarization of nuclei. *Pis'ma Zh. Eksp. Teor. Fiz.* 24:37–39

Bae, M. H., H. J. Lee and J. H. Choi. 2007. Josephson-vortex-flow terahertz emission in layered High-T_c superconducting single crystals. *Physical Review Letters* 98:027002

Barbara, P., A. B. Cawthorne, S. V. Shitov and C. J. Lobb. 1999. Stimulated Emission and Amplification in Josephson junction Arrays. *Physical Review Letters* 82:1963

Bardeen, J., L. N. Cooper and J. R. Schrieffer. 1957. The Theory of Superconductivity. *Physical Review Letters* 108:1175.

Batov, I. E., X. Y. Jin, S. V. Shitov, Y. Koval, P. Muller and A. V. Ustinov. 2006. Detection of 0.5 THz radiation from intrinsic $Bi_2Sr_2CaCu_2O_{8+x}$ Josephson junctions. *Applied Physics Letters* 88:262504.

Bednorz, J. G. and K. A. Müller. 1986. Possible high-Tc superconductivity in the Ba-La-Cu-O system. *Zeitschrift Physics B* 64:189.

Buckel, W. and R. Kleiner, eds. 2004. Superconductivity Fundamentals and Application. Tübingen: *Wiley-VCH* Verlag GmbH and Co. KGaA Weinheim.

Bulaevskii, L. N. and A. E. Koshelev. 2007. Radiation due to Josephson Oscillations in Layered Superconductors. *Physical Review Letters* 99:057002

Chu, C. W., P. H. Hor, R. L. Meng, L. Gao, Z. J. Huang and Y. Q. Wang. 1987. Evidence for superconductivity above 40 K in the La-Ba-Cu-O compound system. *Physical Review Letters* 58:405–407

Esaki, L. 1957. New Phenomenon in Narrow Germanium p-n Junctions. *Physical Review* 109:603.

Fischer, B., M. Hoffmann, H. Helm, G. Modjesch and P. U. Jepsen. 2005.Chemical recognition in terahertz time-domain spectroscopy and imaging. *Semiconductor Science and Technology* 20:S246–S253

Fu, C. C., Z. Huang and N. C. Yeh. 2002. Spin-polarized quasiparticle transport in cuprate superconductors. *Physical Review B* 6(22):224516

Gaifullin, M. B., M. Matsuda, N. Chikumoto, J. Shimoyama and K. Kishio. 2000. Abrupt Change of Josephson Plasma Frequency at the Phase Boundary of the Bragg Glass in $Bi_2Sr_2CaCu_2O_{8+\delta}$. *Physical Review Letters* 84:2945

Gao, L., Y. Y. Xue, F. Chen, Q. Xiong, R. L. Meng, D. Ramirez, C. W. Chu, J. H. Eggert and H. K. Mao. 1994. Superconductivity up to 164 K in $HgBa_2Ca_{m-1}Cu_mO_{2m+2+\delta}$ (m=1,2 and 3) Under Quasihydrostatic Pressures. *Physical Review B* 50:4260

Giaever, I. 1960. Electron tunneling between two superconductors. *Physical Review Letters* 5:464.

Giaever, I. 1965. Detection of the ac Josephson Effect. *Physical Review Letters* 14:904.

Ginzburg, V. L. and L. D. Landau. 1950. On the theory of superconductivity. *Journal of Experimental and Theoretical Physics* 20:1064.

Gray, K. E. 1981. Plenum, New York. For a collection of review articles, see Nonequilibrium Superconductivity, Phonons, and Kapitza Boundaries, *Vol. 65 of NATO Advanced Study Institute, Series B: Physics*

Gray, K.E., L. Ozyuzer, A.E. Koshelev, C. Kurter, K. Kadowaki, T. Yamamoto, H. Minami, H. Yamaguchi, M. Tachiki, W.K. Kwok and U. Welp. 2009. Emission of Terahertz Waves from Stacks of Intrinsic Josephson Junctions. *IEEE Transactions on Applied Superconductivity* 19:886

Hazen, R. M., L. W. Finger, R. J. Angel, C. T. Prewitt, N. L. Ross, C. G. Hadidiacos, P.J. Heaney, D.R. Veblen, Z.Z. Shenh, A. El Ali and A.M. Hermann. 1988. 100 K superconducting phases in the Tl-Ca-Ba-Cu-O system. *Physical Review Letters* 60:1657.

Irie, A., Y. Hirai and G. Oya. 1998. Fiske and flux-flow modes of the intrinsic Josephson junctions in Bi2Sr2CaCu2Oy mesas. *Applied Physical Letters* 72:2159

Ishibashi, T., K. Sato, K. Yonemitsu, K. Sato, K. Lee and S. Kim. 2001. Spin tunneling in Co/Au/I/BiSrCaCuO tunnel junctions. *Superconductor Science & Technology* 14:1014-1017

Jain, A. K., K. K. Likharev, J. E. Lukens and J. E. Sauvageau. 1984. Mutual phase-locking in Josephson junction arrays. *Physics Reports* 109:309

Josephson, B. D. 1962. Possible new effects in superconductive tunneling. *Physics Letter* 1:251-253.

Josephson, B. D. 1964. Coupled Superconductors. *Review of Modern Physics* 36:216–220

Josephson, B. D. 1974. The discovery of tunnelling supercurrents. *Review of Modern Physics* 46(2):251-254

Kadowaki, K., I. Kakeya, T. Yamamoto, T. Yamazaki, M. Kohri and Y. Kubo. 2006. Dynamical properties of Josephson vortices in mesoscopic intrinsic Josephson junctions in single crystalline $Bi_2Sr_2CaCu_2O_{8+d}$. *Physica C* 437-438:111-117

Kadowaki, K., H. Yamaguchi, K. Kawamata, T. Yamamoto, H. Minami, I. Kakeya, U. Welp, L. Ozyuzer, A. Koshelev, C. Kurter, K. E. Gray and W. K. Kwok. 2008. Direct observation of terahertz electromagnetic waves emitted from intrinsic Josephson junctions in single crystalline $Bi_2Sr_2CaCu_2O_{8+d}$. *Physica C* 468:634-639

Kadowaki, K., M. Tsujimoto, K. Yamaki, T. Yamamoto, T. Kashiwagi, H. Minami, M. Tachiki and R. A. Klemm. 2010. Evidence for a Dual-Source Mechanism of Terahertz Radiation from Rectangular Mesas of Single Crystalline $Bi_2Sr_2CaCu_2O_{8+\delta}$ Intrinsic Josephson Junctions. *Journal of the Physical Society of Japan* 79:023703

Kamihara, Y., H. Hiramatsu, M. Hirano, R. Kawamura, H. Yanagi, T. Kamiya and H. Hosono. 2006. Iron-based layered superconductor: LaOFeP. *Journal of the American Chemical Society* 128, 10012–10013

Kawase, K. 2004. Terahertz imaging for drug detection & large scale integrated circuit inspection. *Optics & Photonics News* 15:34–39

Kleiner R., F. Steinmeyer, G. Kunkel, and P. Müller. 1992. Intrinsic Josephson effects in $Bi_2Sr_2CaCu_2O_8$ single crystals. *Physical Review Letters* 68:2394.

Kleiner, R. 1994. Two-dimensional resonant modes in stacked Josephson junctions. *Physical Review B* 50:6919.

Koshelev, A. E. and I. Aranson. 2001. Dynamic structure selection and instabilities of driven Josephson lattice in high-temperature superconductor. *Physical Review B* 64:174508

Koshelev A. E. and L. N. Bulaevskii. 2008. Resonant electromagnetic emission from intrinsic Josephson junction stacks with laterally modulated Josephson critical current. *Physical Review B* 77:014530

Krasnov, V. M. 2006. Quantum Cascade Phenomenon in $Bi_2Sr_2CaCu_2O_{8+\delta}$ Single Crystals. *Physical Review Letters* 97:257003

Kume, E. I., Iguchi, and H. Takahashi. 1999. On-chip spectroscopic detection of terahertz radiation emitted from a quasiparticle-injected nonequilibrium superconductor using a high-T_c Josephson junction. *Applied Physics Letters* 75:2809

Kurter, C., K. E. Gray, J. F. Zasadzinski, L. Ozyuzer, A. E. Koshelev, Q. Li, T. Yamamoto, K. Kadowaki, W. K. Kwok, M. Tachiki and U. Welp. 2009. Thermal Management in Large Bi2212 Mesas Used for Terahertz Sources. *IEEE Transactions on Applied Superconductivity* 19:428

Langenberg, D. N., D. J. Scalapino, B. N. Taylor, and R. E. Eck. 1965. Investigation of Microwave Radiation Emitted by Josephson Junctions. *Physical Review Letter* 15:294.

Lin, S. and X. Hu. 2008. Possible Dynamic States in Inductively Coupled Intrinsic Josephson Junctions of Layered High-T_c Superconductors. *Physical Review Letters* 100:247006.

Lukens, J. 1990. Superconducting Devices, *Plenum Press* p-135

Maeda, H., T. Tanaka, M. Fukutomi and T. Asano. 1988. A New high-Tc oxide superconductor without a rare earth element. *Japanese Journal of Applied Physics* 27:L209.

Madsen, S., G. Fillatrella, and N. F. Pedersen. 2004. Interaction between a BSCCO-type intrinsic Josephson junction and a microwave cavity. *European Physical Journal B* 40:209

Maxwell, E. 1950. Isotope Effect in the Superconductivity of Mercury. *Physical Review* 78:477.

Meissner, W. and R. Ochsenfeld. 1933. Ein neuer effect bei eintritt der supraleitfahigkeit. *Naturwissenschaften* 21(44):787

Minami, H., I. Kakeya, H. Yamaguchi, T. Yamamoto and K. Kadowaki. 2009. Characteristics of terahertz radiation emitted from the intrinsic Josephson junctions in high-T_c superconductor $Bi_2Sr_2CaCu_2O_{8+\delta}$. *Applied Physics Letters* 95:232511

Miyakawa, N., P. Guptasarma, J.F. Zasadzinski, D.G. Hink and K.E. Gray. 1998. Strong dependence of the Superconducting gap on oxygen doping from tunneling measurements on $Bi_2Sr_2CaCu_2O_{8+x}$. *Physical Review Letters* 80:157.

Mott, N. F. 1936a. The electrical conductivity of transition metals. *Proceedings of the Royal Society* 153:699–717

Nagamatsu, J., N. Nakagawa, T. Muranaka, Y. Zenitani and J. Akimitsu. 2001. Superconductivity at 39 K in magnesium diboride. *Nature* 410:63-64

Onnes, H. K. 1911. Disappearance of the electrical resistance of mercury of Helium temperature. *Akad. Van Wetenschappen* (Amsterdam) 14:113.

Ozdemir, M. 2006. Spin polarized tunneling spectroscopy of intercalated $Bi_2Sr_2CaCu_2O_{8+\delta}$. *Izmir Institute of Technology Thesis of M.S*

Ozyuzer, L., A. E. Koshelev, C. Kurter, N. Gopalsami, Q. Li, M. Tachiki, K. Kadowaki, T. Tamamoto, H. Minami, H. Yamaguchi, T. Tachiki, K. E. Gray, W. K. Kwok and U. Welp. 2007. Emission of coherent THz radiation from superconductors. *Science* 318:1291

Ozyuzer, L., Y. Simsek, H. Koseoglu, F. Turkoglu, C. Kurter, U. Welp, A. E. Koshelev, K. E. Gray, W. K. Kwok, T. Yamamoto, K. Kadowaki, Y. Koval, H. B. Wang, and P. Müller. 2009. Terahertz wave emission from intrinsic Josephson junctions in high-T_c superconductors. *Superconductor Science & Technology* 22:114009

Poole, C. P., A. F. Horacio and J. C. Richard. 1995. Superconductivity, *Academic Press*, California

Reynolds, C. A., B. Serin, W. H. Wright, and L. B. Nesbitt. 1950. Superconductivity of Isotopes of Mercury. *Physical Review* 78:487.

Romano, P., J. Chen and J. F. Zasadzinski. 1998. Josephson and Quasiparticle Tunneling in SIS Junctions $Bi_2Sr_2CaCu_2O_8$ and $Bi_2Sr_2CuO_6$. *Physica C* 295:15

Saldin, E. L., E. A. Schneidmiller and M. V. Yurkov. 2000. The Physics of Free ElectronLasers, Advanced Texts in Physics. New York: *Springer-Verlag*, Berlin.

Schilling, A., M. Cantoni, J. D. Guo and H. R. Ott. 1993. Superconductivity above 130 K in the Hg-Ba-Ca-Cu-O System. *Nature* 363:56.

Schmid, A. and G. Schön. 1975. Linearized kinetic equations and relaxation processes of a superconductor near T_c. *Journal of Low Temperature Physics* 20:207

Shapiro, S. 1963. Josephson currents in superconducting tunneling: the effect of microwaves and other observations. *Physical Review Letters* 11:80

Suziki, M., T. Watanabe and A. Matsuda. 1999. Short pulse tunneling measurements of intrinsic Josephson junction in Bi-Sr-Ca-O. *IEEE Transactions on Applied Superconductivity* 9:4507

Suzuki, M., T. Hamatani, Y. Yamada, K. Anagawa and T. Watanabe. 2009. Significantly doping-dependent Josephson critical current–Inhomogeneity in real space or heterogeneity in k-space. *Journal of Physics: Conference Series* 150:052252

Tachiki, M., S. Fukuya and T. Koyama. 2009. Mechanism of Terahertz Electromagnetic Wave Emission from Intrinsic Josephson Junctions. *Physical Review Letters* 102:127002

Taillefer, L., B. Lussier, R. Gagnon, K. Behnia, and H. Aubin. 1997. Universal heatconduction in YBa_2Cu_3O6. *Physical Review Letters* 79:483–486

Takahashi, H., K. Igawa, K. Arii, Y. Kamihara, M. Hirano and H. Hosono. 2008. Superconductivity at 43 K in an iron-based layered compound LaO1-xFxFeAs. *Nature* 453(7193): 376–378

Tanabe, K., Y. Hidaka, S. Karimoto and M. Suzuki. 1996. Observation of both pair and quasiparticle tunneling in intrinsic junction stacks fabricated on $Bi_2Sr_2CaCu_2O_{8+x}$ single crystals. *Physical Review B* 53:9348

Tedrow, P. M., and R. Meservey. 1973. Spin polarization of electrons tunneling from films of Fe, Co, Ni, Gd. *Physical Review B* 7:318–326

Tinkham, M. 1996. Introduction to Superconductivity, 2nd ed. *McGrawHill*, New York

Tonouchi, M. 2007. Cutting-edge terahertz technology. *Nature Photonics* 1:97-105

Wade, A., G. Fedorov, D. Smirnov, S. Kumar, B. S. Williams, Q. Hu and J. L. Reno 2009. Magnetic-field-assisted terahertz quantum cascade laser operating up to 225 K. *Nature Photonics* 3:41

Wang H. B., S. Guenon, J. Yuan, A. Iishi, S. Arisawa, T. Hatano, T. Yamashita, D. Koelle and R. Kleiner. Hot Spots and Waves in $Bi_2Sr_2CaCu_2O_8$ Intrinsic Josephson Junction Stacks: A Study by Low Temperature Scanning Laser Microscopy. 2009. *Physical Review Letters* 102:017006

Watanabe T., T. Fuji and A. Matsuda. 1997. Anisotropic Resistivities of Precisely Oxygen Controlled Single-Crystal $Bi_2Sr_2CaCu_2O_{8+\delta}$: Systematic Study on "Spin Gap" Effect. *Physical Review Letters* 79:2113

Wesche, R. 1998. High Temperature Superconductor Materials, Properties, and Application. Boston: *Academic Publishers*

Wu, M. K., J. R. Ashburn, , C. J. Torng, P. H. Hor, R. L. Meng, L. Gao, Z. J. Huang, Y. Q. Wang and C. W. Chu. 1987. Superconductivity at 93 K in a New Mixed-Phase Y-Ba-Cu-O Compound System at Ambient Pressure. *Physical Review Letters* 58:908

Yurgens, A., D. Winkler, N. V. Zavaritski and T. Claeson. 1996a. Strong temperature dependence of the c-axis gap parameter of $Bi_2Sr_2CaCu_2O_{8+x}$ intrinsic Josephson junctions. *Physical Review B* 53:R8887.

Yurgens, A. 2000. Intrinsic Josephson junctions: Recent developments. *Superconductor Science and Technology* 13:R85-100.

Yurgens, A., D. Winkler, T. Claeson, S. Ono and Y. Ando. 2004. Yurgens et al. Reply. *Physical Review Letters* 92:259702

Zasadzinski, J. 2002. Tunneling spectroscopy of conventional and unconventional superconductors: The Physics of Superconductor, Edited by Bennemann, K., H. and Ketterson, J. New York: Springer

Zhi-An, R., L. Wei, Y. Jie, Y. Wei, S. Xiao-Li, Z. Cai, C. Guang-Can, D. Xiao-Li, S. Li-Ling, Z. Fang and Z. Zhong-Xian. 2008. Superconductivity at 55 K in Iron-Based F-Doped Layered Quaternary Compound $Sm[O_{1-x}F_x]FeAs$. *Chinese Physics Letters* 25(6):2215

Zhu, X. B., Y. F. Wei, S. P. Zhao, G. H. Chen, H. F. Yang, A. Z. Jin, and C. Z. Gu. 2006. Intrinsic tunneling spectroscopy of $Bi_2Sr_2CaCu_2O_{8+\delta}$: The junction-size dependence of self-heating. *Physical Review B* 73:224501